

1 **A new accurate low-cost instrument for fast synchronized spatial measurements of light**
2 **spectra**

3 Bert G. Heusinkveld, Wouter B. Mol, Chiel C. van Heerwaarden

4 *Meteorology and Air Quality Group, Wageningen University & Research, P.O. Box 47, 6700 AA*
5 *Wageningen, The Netherlands*

6 **Abstract**

7 We developed a cost-effective Fast Response Optical Spectroscopy Time synchronized instrument
8 (FROST). FROST can measure 18 light spectra in 18 wavebands ranging from 400 to 950 nm with a 20
9 nm full width half maximum bandwidth. The FROST 10 Hz measurement frequency is time-synchronized
10 by a Global Navigation Satellite System (GNSS) timing pulse and therefore multiple instruments can be
11 deployed to measure spatial variation of solar radiation in perfect synchronization. We show that FROST
12 is capable of measuring global horizontal irradiance (GHI) despite its limited spectral range.

13 It is very capable of measuring Photosynthetic Active Radiation (PAR) because 11 of its 18 wavebands
14 are situated within the 400 to 700 nm range. A digital filter can be applied to these 11 wavebands to
15 derive the Photosynthetic Photon Flux Density (PPFD) and retain information of the spectral composition
16 of PAR radiation.

17 The 940 nm waveband can be used to derive information about atmospheric moisture.

18 We showed that the silicon sensor has undetectable zero offsets for solar irradiance settings and that the
19 temperature dependency as tested in an oven between 15°C and 46°C appears very low (-250 ppm K^{-1}).
20 For solar irradiance applications, the main uncertainty is caused by our Poly Tetra Fluor Ethylene (PTFE)
21 diffuser (Teflon), a common type of diffuser material for cosine-corrected spectral measurements. The
22 oven experiments showed a significant jump in PTFE transmission of 2% when increasing its temperature
23 beyond 21°C.

24 The FROST total cost ($<€200$) is much lower than current field spectroradiometers, PAR sensors or
25 Pyranometers, and includes a mounting tripod, solar power supply, datalogger and GNSS and waterproof
26 housing. The FROST is a fully stand-alone measurement solution. It can be deployed anywhere with its
27 own power supply and can be installed in vertical in-canopy profiles as well. This low cost makes it
28 feasible to study spatial variation of solar irradiance using large grid high-density sensor set-ups or to
29 use FROST to replace existing PAR sensor for detailed spectral information.

30 **1. Introduction**

31 Understanding solar irradiance and its interaction with clouds and vegetation is of utmost importance to
32 unravel the complexity of feedback systems that determine our weather and climate. Cloud-shading
33 dynamics of irradiance are highly dynamic (Lohmann, 2018) and Cloud-Resolving Models (CRM) are
34 unable to resolve short time intervals and small spatial scales. At grid scales below 1 km, 3-D radiative
35 transfer models can greatly improve the 3-D surface and atmosphere heating rates in atmospheric
36 models (Calahan et al., 2005, Jakub & Mayer, 2015). A good example is the complexity of the radiative
37 effects of shallow cumulus clouds and its interactions with a vegetated surface. Traditional 1-D radiation
38 models produce unrealistic surface radiation fields but Menno et al. (2020) showed that a 3-D radiation
39 transfer model could greatly improve the coupling mechanisms between clouds and the land surface. The
40 small circulations, turbulence and combined cloud microphysics in convective boundary layers are both
41 highly non-linear and complex. CRMs are crucial for improving weather forecasting models and for the
42 energy meteorology sector. Kreuwel et al. (2020) showed that solar powered grid loading is highly
43 dynamic and especially so for smaller household PV systems, leading to grid overload challenges at very
44 short time intervals of seconds. High quality observations, both in high resolution spatially and with a
45 high temporal resolution, are required to test such models but so far observations are lacking (Guichard
46 and Couvreur, 2017).

47 Yordanov et al. (2013) showed that cloud enhancements can significantly increase solar irradiance levels
48 (>1.5 times), which result in peak irradiance levels well exceeding extraterrestrial levels even at high
49 altitudes and latitudes (Yordanov, 2015). They used fast response silicon sensors and their highest
50 detected irradiance bursts lasted about 1 s, which led them to believe that the required light sensor
51 response time should be at least 0.15 s, much faster than traditional thermopile pyranometers with a
52 response time of several seconds. The slow response time of those thermopile sensors is related to the
53 thermal mass of the thermopile sensor. Semiconductor light sensors respond faster because photons
54 directly mobilize electrons that can be measured directly. The downside of semiconductor light sensors is
55 their limited and non-flat spectral response and temperature sensitivity. Thermopile based pyranometers
56 are also expensive as compared to a silicon-based solution, which limits their large-scale use in
57 meteorological measurement networks. Martinez et al. (2009) showed that a factor of 10 reduction in
58 pyranometer costs as compared to a thermopile sensor is possible with the use of a silicon photodiode,
59 however their spectral response is limited (400 to 750 nm) and it has non-flat spectral response. A major
60 solar spectral change occurs in the infrared due to water absorptions bands, which leads to an
61 overestimation for clear sky conditions and an underestimation for overcast skies when calibrated for
62 average weather conditions.

63 The spectral response limitations of the photodiode used by Martinez et al. (2009) can be improved with
64 a wider spectral response silicon type pyranometer such as applied in the LI-COR 200-SZ as
65 demonstrated by Michalsky et al. (1991). They compared the LI-COR 200-SZ with a thermopile
66 pyranometer (Kipp & Zonen CM-11). The CM-11 has a flat spectral response (300 to 2500 nm) whereas
67 the LI-COR 200-SZ exhibits a very nonlinear and limited spectral response starting at 400 nm and
68 increasing 5-fold in sensitivity towards its peak around 1000 nm, then sharply dropping off to zero at
69 1100 nm (Alados-Arboleda et al., 1995). Their main uncertainty is related to the temperature
70 dependance of silicon sensors. After a temperature correction, they performed similarly to thermopile
71 pyranometers (11.4 W m⁻² rms errors) under clear and cloudy sky conditions. This is surprisingly
72 accurate because LI-COR calibrates their pyranometer against a reference thermopile pyranometer and
73 therefore a change in solar spectrum may affect its accuracy. Michalsky et al. (1990) argued that the
74 clear or cloudy sky global horizontal irradiance (GHI) spectra is similar because of clouds mixing the
75 direct and blue skylight. This, however, is contradicted by a recent study by Durand et al. (2021) where
76 they investigated the spectral differences between clear and overcast skies. They showed that clouds, in
77 relative terms, enrich GHI spectra in wavelengths < 465 nm and is depleted in wavelengths > 465 nm.
78 This may well explain why the LI-COR sensor performed so well because its main sensitivity is in
79 wavelengths > 465 nm thus indirectly correcting for the reduced infrared in the major water absorption
80 bands beyond its spectral range.

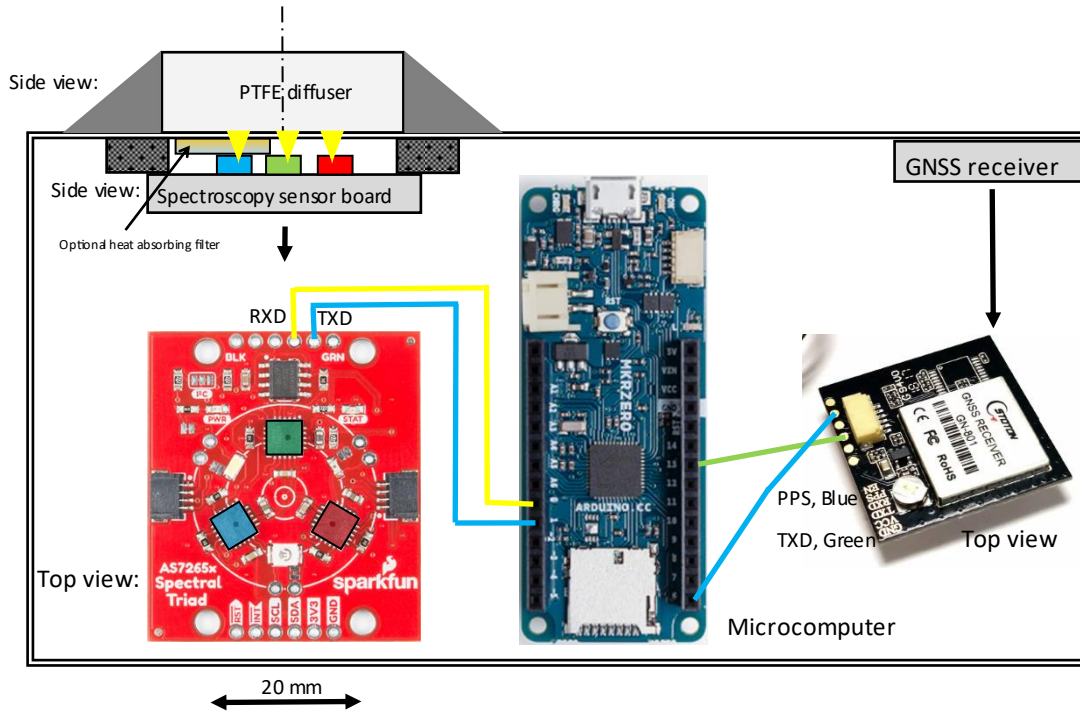
81 Optoelectronics are evolving rapidly and innovations in semiconductor integration with optical
82 components and microprocessors are paving the way for cost-effective spectrometers that can provide
83 even temperature-compensated spectral details about solar radiation. A leading manufacturer in this field
84 is AMS (Austria Micro Systems, Austria) and offers various intelligent light sensing products that are
85 capable of measuring light intensity within multiple optical wavebands. These sensors are mass-
86 produced, resulting in low-cost sensors. Tran and Fukuzawa (2020), tested such a cost-effective 18 band
87 multispectral sensor (AS7265x, AMS) for spectroscopy of fruit (between 400 and 950 nm) and useful
88 information could be derived. Such filter spectroscopy sensors would be very interesting for solar global
89 horizontal irradiance measurements (GHI). The spectral signature of radiation is very relevant to quantify
90 since clouds and air pollution modify the solar light spectrum and light scattering. Additionally, multiple
91 reflections between various ground and water surfaces and clouds will further influence the light spectral
92 composition. This is especially relevant in the photosynthetic active radiation wavelengths (PAR) for
93 vegetation cloud feedbacks since it affects photosynthesis and evapotranspiration (Durand et al., 2021).

94 Here we present the development of a cost-effective fast-response solar light sensor grid for spatially
95 and temporally high resolution multiple light waveband-resolved GHI measurements. The required large
96 number of sensors requires cost-effective design optimization.

97 Additionally, we tested these sensors for meteorological, photosynthesis and remote sensing applications
 98 as well as performance both in the lab and in field experiments.

99 **2. Instrument design and measurement method**

100 The measurement system we developed is depicted in Fig. 1 and consists of a silicon light sensor chipset
 101 (AMS AS7265x), a GNSS for time synchronization, a cosine corrector light diffusing input port, and a
 102 microcomputer. See Table 1 for a list of components.



103

104 Figure 1: Mechanical layout and wiring diagram of the FROST spectrometer (Sensor: 3.2 mm below a
 105 Teflon filter with radius of 32 mm). For easy identification we color-coded the three light sensors (blue,
 106 green and red), each measuring 6 channels.

107 Time-synchronized measurements are achieved using a hardware GNSS receiver timing pulse (PPS) to
 108 trigger each measurement and time-stamped data is processed and collected by a microcomputer board
 109 (Fig. 1, Table 1).

110 Table 1: List of components for the waterproof solar powered spectrometer.

Component	Manufacturer and model	Price (€)
Spectroscopy chipset	AS7265x spectral sensors triple AMS (Austria) with interfacing logic mounted on a PCB by Sparkfun (U.S.A.)	70.00
Optical filter	Schott heat-absorbing colored glass filter KG3 or KG1, 2 mm (Germany)	11.00
UV-sensor	GUVA-S12SD (optional, with a thin second PTFE diffuser)	1.70
PTFE diffuser	32 mm diameter, cut from a plate (S-Polytec GmbH, Germany)	3.00
GNSS receiver	TOPGNSS GN-901, China, GPS and Glonas receiver	6.00
Microcomputer	Arduino MKR Zero	23.00
Memory card	Kingston Canvas Select Plus microSDHC 32GB	4.00
Breadboard	Solderless PCB breadboard Mini protoboard	0.90
Solar panel	First Solar, China, CNC165x165-5, Polycrystalline, 4.2 W, 5 V, 840 mA, 165x165 mm	7.00
Battery	Li-Ion battery LP906090JH, Jauch, Germany	30.00
Charger controller	Mini Solar Lipo Charger board CN3065	1.40

Box	Outdoor Junction Box 100x150x70mm waterproof IP65, Shockproof ABS plastic. ManHua, China (AliExpress)	9.00
Tripod mount adapter	Camera metal shoe mount adapter 1/4" thread	0.75
Tripod	König KN-TRIPOD21/4 camera tripod pan & tilt 130 cm	12.00
Ground anker	Tent herring	1.00
Silicone adhesive sealant	Permatex 81158 or Bizon Black Silicone Adhesive	1.00

111

112 The light sensors are mounted on camera tripods, which makes leveling easy (Fig. 2). A camera metal
 113 shoe mount adapter was glued under the polycarbonate housing for fast mounting. For winds >6 m/s it
 114 is advised to use tent herrings to fix the tripod to the ground. The power consumption is 0.5 W and a 6
 115 Ah LiPo battery will last for 40 h without sunshine. Battery capacity is reduced at lower temperatures.
 116 The 4.2 W polycrystalline solar panel together with a LiPo charge regulator is a reliable power supply
 117 solution for continuous operation in the Dutch climate from April - September. The solar panel is glued
 118 on a special shaped wooden frame that slides over the tripod center tube, with the solar panel sides
 119 resting against the two outer tripod leg (Fig. 2). It is fixed to the rear leg with a thin metal wire. Hot glue
 120 appeared unsuitable for the panels and it is advised to use epoxy glue.

121 The PTFE diffuser was glued to the box by roughening the surfaces and using a black silicone adhesive
 122 around the diffuser edges.



123

124 Figure 2: FROST with solar panel mounted on a camera tripod.

125 The correct synchronization of the sensor grid measurements is essential and several options were
 126 considered such as a network configuration with synchronized triggering at fixed time intervals. Wires in
 127 the field were not an option due to logistic challenges, and radio communication could be possible but
 128 adds to the cost with reduced reliability due to radio interference. As a robust option, a GNSS receiver
 129 was chosen that constantly synchronizes its internal time to an international clock standard. Similar
 130 timing synchronizations are used for sensors grids in seismic activity monitoring of volcanos where

131 timing is essential to determine seismic propagation and where synchronization accuracy of 50 ns could
132 be achieved (Lopez Pereira et al., 2014).

133

134 **2.1 Light sensor**

135 The light sensing element is the AMS AS7265x, a smart spectrometer sensor capable of measuring light
136 at 18-Channel 20 nm full width half maximum (FWHM) bandwidth from visible and near infrared spectral
137 bands (410 to 940 nm) with an electronic shutter (manufacturer: AMS, Australia). It has a broad
138 operational temperature range from -40°C to 85°C. The spectrometer consists of three separate
139 integrated circuits with each including six silicon-based photo diodes with integrated optical bandpass
140 interference filters, micro-lenses, a programmable analog amplifier, and an analog to digital converter
141 and a microprocessor. We will identify the AS72651, -52, -53 as the blue, red and green sensor, as
142 indicated in Fig. 1. The integrated light interference filters are directly deposited on the silicon. Factory
143 calibration values are stored inside the internal memory. Two serial communication options are available
144 for interfacing with a microcomputer; a Universal Asynchronous Transmission (UART) and a synchronous
145 serial transmission (I2C) port. The three light sensor view angles are limited by the chip housing light
146 input port to 41°, which ensures that the optical interference band filters stay within the 20 nm FWHM
147 and +/- 10 nm center-wavelength specifications. AMS states that their filter stability (in time and against
148 temperature) is not detectable but does not provide further specifications. They do mention that the
149 wavelength accuracy is within +/- 10 nm. The AS7265x triple set of light sensor chips, each capturing six
150 light wavebands, poses a challenge to couple optically all three to the same sensing area and to assure a
151 good cosine response needed for the accurate measurement of GHI. The limited opening angle poses an
152 additional challenge for GHI measurements since they require a viewing angle of 180°, therefore an
153 achromatic cosine-corrected diffuser is required.

154 **2.2 Diffuser material**

155 Teflon (PTFE) material is commonly used as an effective light diffuser, with a large spectral transmission
156 range starting below 300 nm, and is available from various manufacturers. However, PTFE light
157 transmittance exhibits a temperature dependency caused by a major phase change in its crystalline
158 structure at 19°C. The phase change can cause a significant change in transmittance. Yliantilla and
159 Schreder (2005), tested three commercially available PTFE diffusers and found transmission changes
160 between 1% and 4% at the phase change temperature. By comparison, they also showed a quartz
161 diffuser with a linear response to temperature (0.035% °C⁻¹) without the sudden transmission jump as
162 found in the PTFE diffusers. Despite this, PTFE was nevertheless chosen as a cost-effective diffuser to
163 maximize the spatial number of sensors. The diffusers were cut from PTFE plates (S-Polytec GmbH,
164 Goch, Germany) using a vice and a hole punch to press round diffusers. A 10.6 and 2.0 mm thick diffuser
165 were tested. The transmission temperature dependency of our PTFE diffusers was tested in a
166 temperature-controlled oven with a cooler (WTS Binder, Germany with a EURO THERM temperature
167 controller). The oven is equipped with a front glass door and the lowest possible temperature setting was
168 kept above the dewpoint temperature of the laboratory to avoid moisture condensation issues. An LED
169 light source (LCS, 17 W, 2500 Lumen) was chosen for its high output and limited thermal infrared and
170 powered by a stabilized voltage power supply. The LED was placed outside the oven in front of the oven's
171 glass door about 1 m away to minimize lamp heating. A second light sensor was placed outside the oven
172 next to the lamp to monitor its output. Diffuser light transmission measurements were corrected for
173 variation in lamp output. Subsequently the light sensor without a diffuser was tested. Temperature
174 sensitivity measurement results are presented in Section 3.2.

175 The spectrometer performance was also tested at the DWD (German Weather Service) radiation
176 calibration facility in Lindenberg, Germany. The spectrometer output was compared against a calibrated
177 xenon light source and the intensity was adjusted by varying the lamp sensor distance between 0.5 m
178 and 0.7 m. The possible spectral crosstalk of infrared light was tested by placing a very steep long pass
179 interference filter with a Cut-On Wavelength of 1000 +/-9 nm (Dielectric Coated Long pass Filter, 25.4

180 mm diameter, 1.1 mm thick, transmission >95%, OD5 Blocking, Edmund optics, Stock #15-463) in front
181 of the sensor. The long pass filter blocks all sensor wavebands and any remaining signal is then
182 considered infrared crosstalk. The position of the optical waveband filters was tested using a Cary 4000
183 (Agilent, USA) UV-Vis NIR spectrophotometer at Wageningen University, The Netherlands. Results are
184 presented in Section 3.1.

185 **2.3 Cosine response**

186 The cosine response was determined by placing a LED light source (LED light bulb 2500 Lumen, diameter
187 0.1 m) and our light sensor 5 m apart, both on tripods at 1 m height. Since a darkroom was not
188 available, the measurements were performed outdoors at night to avoid reflection from ceilings and
189 walls. A night with low humidity was chosen to minimize aerosol light scattering. The direction of the
190 light sensor was adjusted from 0° (viewing the light source) to 90° (perpendicular to the light beam). To
191 keep the distance between the sensor and light source constant during rotation, the plane of rotation was
192 exactly located at the diffuser surface. A shading screen was placed between the light source and sensor
193 to shade the ground surface to avoid any light reflection into the sensor. Results are presented in Section
194 3.3.

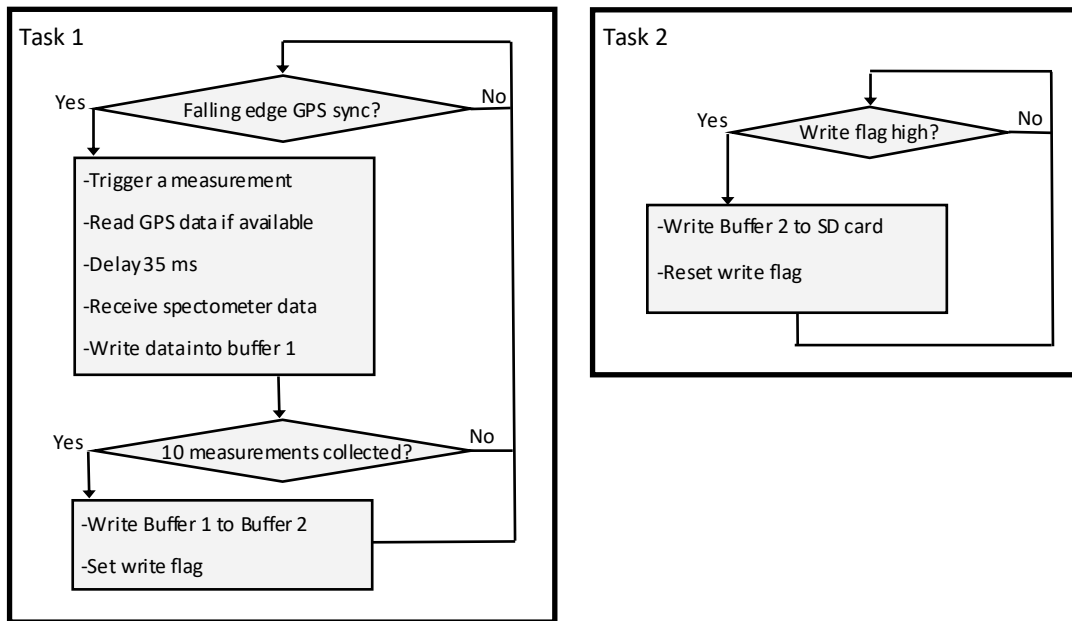
195 **2.4 Time synchronization**

196 Instead of using a GNSS for synchronizing an internal clock or using the serial date and time output, we
197 use the very precise (<100 ns accuracy) hardware timing pulse of a GNSS module to trigger each
198 measurement directly (at 10 Hz.). The data is time-stamped with the GNSS date and time output. A
199 special GNSS receiver was selected that also outputs a programmable timing pulse for synchronization
200 purposes (better than 50 ns). As a bonus, it also provides location data within a few meters. These
201 receivers can be purchased for less than 6€ (Table 1). The time synchronization analysis can be found in
202 Section 3.4.

203 **2.5 Datalogging**

204 The datalogging of the GNSS date, time, latitude, longitude and the 18 channel spectroscopy
205 measurements at 10 Hz results in a dataflow of >100 MB data per day. The spectroscopy sensor outputs
206 ASCII data and the bandwidth of the I2C interface on the spectroscopy side were insufficient, thus the
207 UART serial interface was selected. The sensor can be triggered by serial command to do a measurement
208 and this command in turn is triggered by the hardware timing pulse of the GNSS.

209 For datalogging, the MKR Zero of the Arduino family microprocessor platforms was chosen. It is a cost-
210 effective and low power datalogging solution using a 48 MHz SAMD21 Cortex 32bit low power ARM MCU
211 and a built-in micro-SD card holder (max. 32 GB). A consumer grade 32 GB SD card was selected, data
212 rates are low (<5 KB s⁻¹) and the large size ensures that the card does not wear down fast (<4 GB
213 month⁻¹). The challenge with this datalogging solution is that the default operating system cannot handle
214 sustained data writing to an SD card at 10 Hz using linear programming (despite a low data rate of <5
215 KB s⁻¹). In fact, the SD card would regularly delay the measurements with an estimated 200 ms resulting
216 in a loss of data (tested with a new, fast SD card with 85 MB/s max write speed). Thus it needs a
217 microcontroller multitasking real-time operating system and FreeRTOS (freertos.org) was chosen to
218 overcome this. Two tasks that run semi-parallel on the single core CPU were defined. The first task with
219 the highest priority will initiate a measurement cycle at the falling edge of the hardware timing signal of
220 the GNSS. Task 2 will trigger each second and writes the 10 Hz buffered data to the SD card (Fig. 3).



221

222 Figure 3: Multitasking software implementation for synchronized measurements and data storage. Each
 223 Buffer can contain 10 rows of data. The program is available at zenodo.org (DOI
 224 10.5281/zenodo.6945812).

225 **2.6 Field experiments**

226 The field experiments were conducted at various locations. At the Veenkampen weather station,
 227 Wageningen, The Netherlands (Lat.: 51.981°, Long.: 5.620°), sensor performance was tested against
 228 GHI measurements and a spectrophotometer. Although GHI is directly measured with a pyranometer, it
 229 was decided to use the pyr heliometer and diffuse radiation sum to reduce cosine response errors. The
 230 instruments consist of a Kipp and Zoonen Pyr heliometer CMP1 with a calibration accuracy of +/-0.5%
 231 and a first class pyranometer CM21 for diffuse radiation measurements with a time constant of 5 s,
 232 directional error <+/-10W m², tilt error: +/- 0.2%, zero-offset due to T change: <2 W m² at 5K h⁻¹,
 233 cosine response error: max +/-2% at 60°, max. +/-6% at 80°. Both instruments were mounted on a
 234 suntracker (EKO instruments, Japan, STR-21 with shading disk). On selected days the solar spectrum
 235 was measured with the ASD FieldSpec (U.S.A.) field spectroradiometer with a cosine collector and with a
 236 factory recalibration made in 2021.

237 Additionally, a large set of sensors were deployed during the FESSTVaL campaign (<https://fesstval.de/>)
 238 at the German Weather Service (DWD) in Falkenberg, Germany, to study the spatial variation of solar
 239 irradiance (June 2021). For that campaign, it was crucial to obtain fast and time synchronized spatial
 240 solar irradiance measurements. Their Baseline Surface Radiation Network (BSRN) location at Lindenberg
 241 (Driemel et al., 2018) was used to test long-term stability from 22 June-31 August 2021.

242 The FROST was also deployed in a field experiment in La Cendrosa, Spain (Lat: 41.692537, Long:
 243 0.931540) from 14-29 July 2021. It was used, among other things, to study crop growth.

244 **3. Performance and applications**

245 The performance of the sensor, the temperature dependency and cosine response of the diffuser and the
 246 time synchronization are presented below. The infrared crosstalk is analyzed by measuring signal
 247 response with all light below 1000 nm blocked using a low-pass infrared filter. Subsequently a correction
 248 method using heat absorbing infrared filters (referenced to as "correction filters") is introduced and
 249 tested. This results in three versions of FROST: one with a 10.6 mm diffuser, one with a 2 mm diffuser
 250 including a correction filter on the blue sensor, and one with a 2 mm diffuser with two correction filters
 251 (on the blue and red sensor).

252 **3.1 Spectral response and calibration**

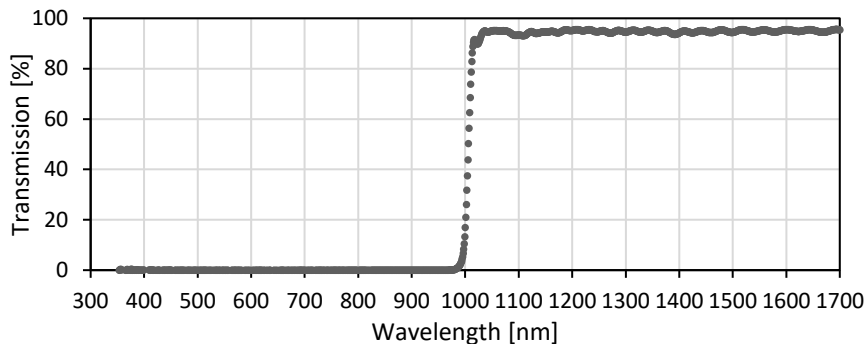
253 According to the manufacturer specifications, the normalized (at peak wavelength) responsivity of their
254 spectroradiometer has a good narrow band response (20 nm full width half maximum (FWHM)) and
255 limited overlap for the 18 channels. Wavelength accuracy is within +/- 10 nm and this was confirmed by
256 testing the sensor inside a Cary 4000 UV-Vis spectrophotometer equipped with a universal attachment
257 accessory. Unfortunately, the Cary spectrophotometer had a limited spectral range so we could not test
258 the crosstalk in the near infrared, nor the 940 nm band (Fig. 6a).

259 Linearity was tested by comparing the spectroradiometer against a reference thermopile pyranometer
260 CM21 (Kipp and Zoonen, The Netherlands) and a stabilized halogen light source in a dark room. The
261 intensity was adjusted by changing the lamp distance. The FROST non-linearity was at least as good as
262 the CM21, which has a non-linearity of <+/-0.2%. The factory-calibrated accuracy is +/- 12% according
263 to the manufacturer specifications (in counts/ $\mu\text{W}/\text{cm}^2$). After initial testing using solar radiation as a light
264 source for reflectance measurements of lawn grass, we were confronted with unusual data. The PAR
265 region clearly showed very high reflection values, more than 5 times of what is typical for such a surface.

266 After consultation with the manufacturer (AMS), they clarified that the AS72653 sensor has a strong
267 crosstalk in the near infrared. The sensor was meant to be used with LED light for spectral reflectance
268 measurement applications, which would not produce light > 1000 nm. They recommend for each sensor
269 a specific LED, and therefore each reflectance measurement would consist of 3 separate measurements
270 with each using one sensor and with one specific LED at a time.

271 We tested the sensor at the DWD radiation calibration facility in Lindenberg using a calibrated light
272 source. The crosstalk caused by light wavelengths beyond 1000 nm was measured by using an optical
273 Long Pass interference (LP) filter that blocks all light below 1000 nm. Thus, the remaining signal on all
274 18 channels can be attributed to a crosstalk from wavelengths >1000 nm. The blocking filter
275 characteristics were tested in a Cary 5000 UV-Vis-NIR spectrophotometer equipped with a universal
276 attachment accessory (Fig. 4).

277

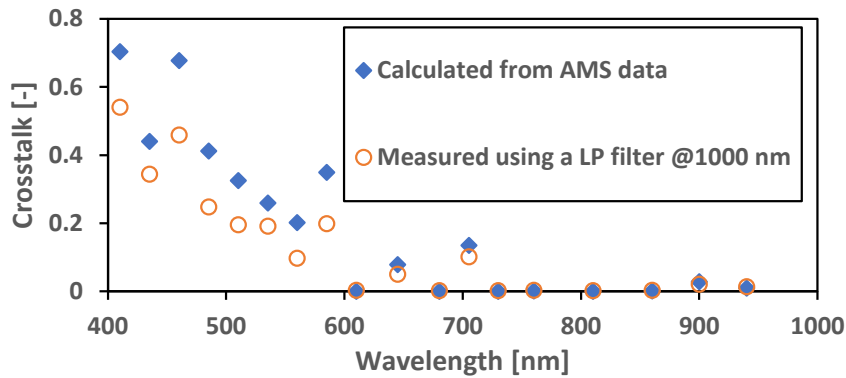


278

279 Figure 4: Transmission of the optical LP filter measured with a Cary 5000 UV-Vis-NIR spectrophotometer
280 equipped with a universal measurement accessory at the DWD, Lindenberg, Germany.

281

282

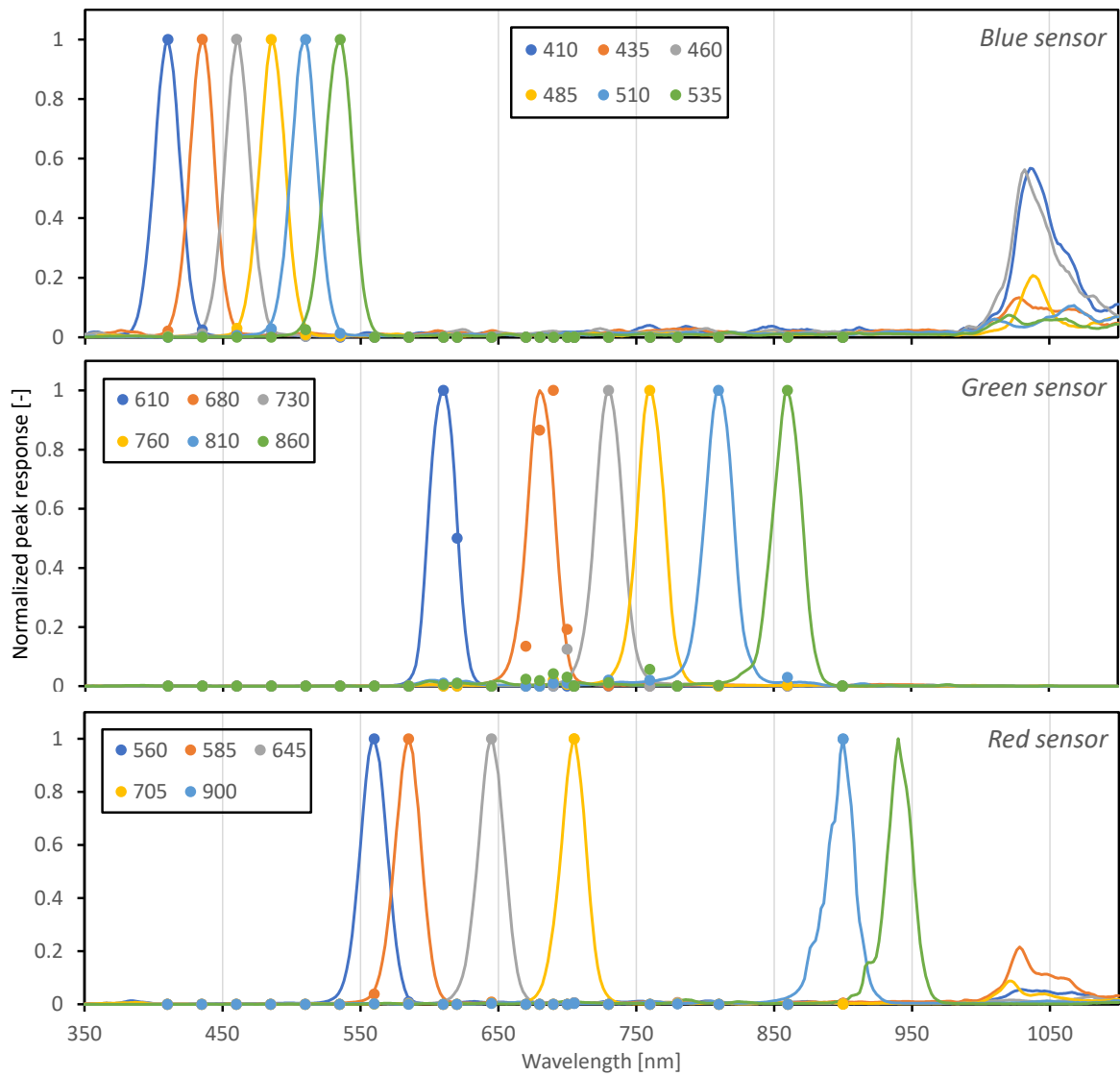


283 Figure 5: Measured spectroscopy sensor infrared crosstalk from wavelengths >1000 nm, tested with a
 284 Xenon lamp and an optical long pass filter (LP at 1000 nm) and calculated from spectral response data as
 285 supplied by the manufacturer (AMS). Crosstalk is defined as the fraction of light wavelengths >1000 nm
 286 the sensor is responding to, for example at 410 nm 55% of the measured signal is actually originating
 287 from wavelengths >1000 nm.
 288

289 Figure 5 shows the fraction of infrared light (>1000 nm) within the sensor output for each of the 18
 290 channels. The sensor output was corrected for the LP filter transmission loss (about 5%, see Fig. 4). Note
 291 that the crosstalk is larger than during solar radiation measurements because a Xenon light source
 292 contains a higher amount of infrared radiation. Cloudy conditions would further reduce crosstalk. For
 293 clear sky conditions, the crosstalk would be about half of the Xenon light. The blue dots in Fig. 5 show
 294 the calculated crosstalk using the AMS sensor spectral filter response data obtained through personal
 295 communication with the manufacturer (Fig. 6a). The measured crosstalk on the blue sensor appears to
 296 be slightly better. The crosstalk is very large in the visible light range and confirms the provided filter
 297 transmission curves from AMS (personal communication). Note that those transmission curves (Fig. 6a)
 298 are not available on the publicly available datasheet. Figure 5 shows that only half of the channels
 299 provide the correct spectral information (if calibrated correctly using the data from Fig. 6a). However,
 300 there are enough channels to measure the so-called red edge around 700 nm in vegetation light
 301 transmission and reflection. This opens up applications for vegetation growth measurements without
 302 further modifications.

303 All channels in the blue sensor and some of the channels (650 and 685 nm) in the red sensor have very
 304 high crosstalk from the 1000 to 1100 nm range, but the crosstalk makes the sensor cover a larger range
 305 of the solar spectrum. It is therefore still usable if this can be quantified.

306



307

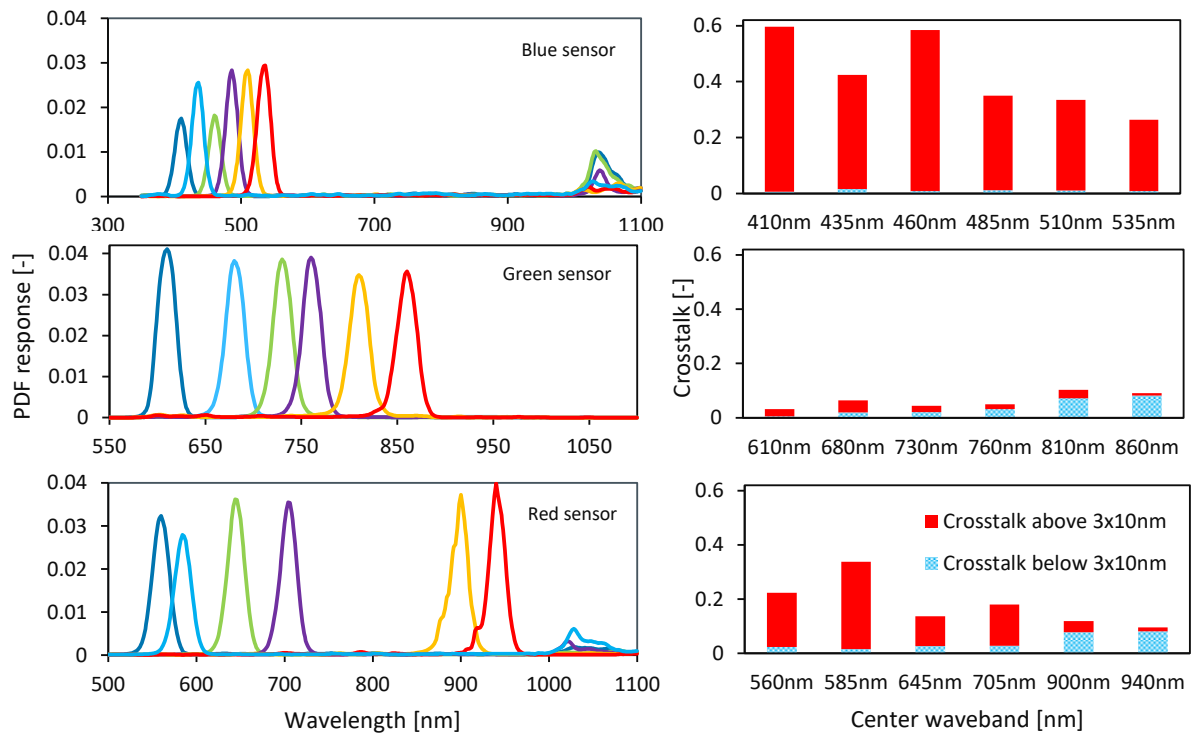
308 Figure 6a: Normalized peak spectral response of the triple AMS sensor (denoted as blue, green and red
 309 sensor), data provided by manufacturer after consultation (solid lines) and our measured response up to
 310 900 nm (dots) as measured with a sensor placed inside a Cary 4000 UV-Vis spectrophotometer equipped
 311 with a universal measurement accessory.

312

313

314

315

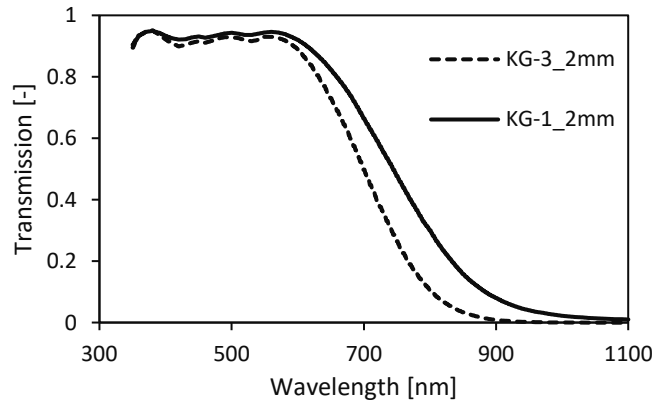


316

317 Figure 6b: Left panels: Spectral response of the triple AMS sensor (denoted as blue, green and red
 318 sensor), Probability Density Functions (PDF) calculated from data provided by manufacturer AMS
 319 (personal communication). Right panels: The crosstalk for each channel is presented as two values:
 320 Signal originating from $>(\text{center wavelength} + 30 \text{ nm})$ divided by total signal of a channel (red) and signal
 321 $<(\text{center wavelength} - 30 \text{ nm})$ divided by total signal of a channel (blue) (sensor only, without diffuser).

322 In Fig. 6b, the right panels, show that the crosstalk for a flat spectrum, defined as the signal above or
 323 below $3 \times 0.5 \text{ FWHM}$ from the center wavelength, is large (up to 60%) in the PAR range for the blue
 324 sensor and mainly from the infrared beyond 1000 nm. The green sensor performs much better and
 325 exhibits minimal infrared crosstalk ($< 5\%$). The red sensor has an issue mainly with the first two
 326 channels.

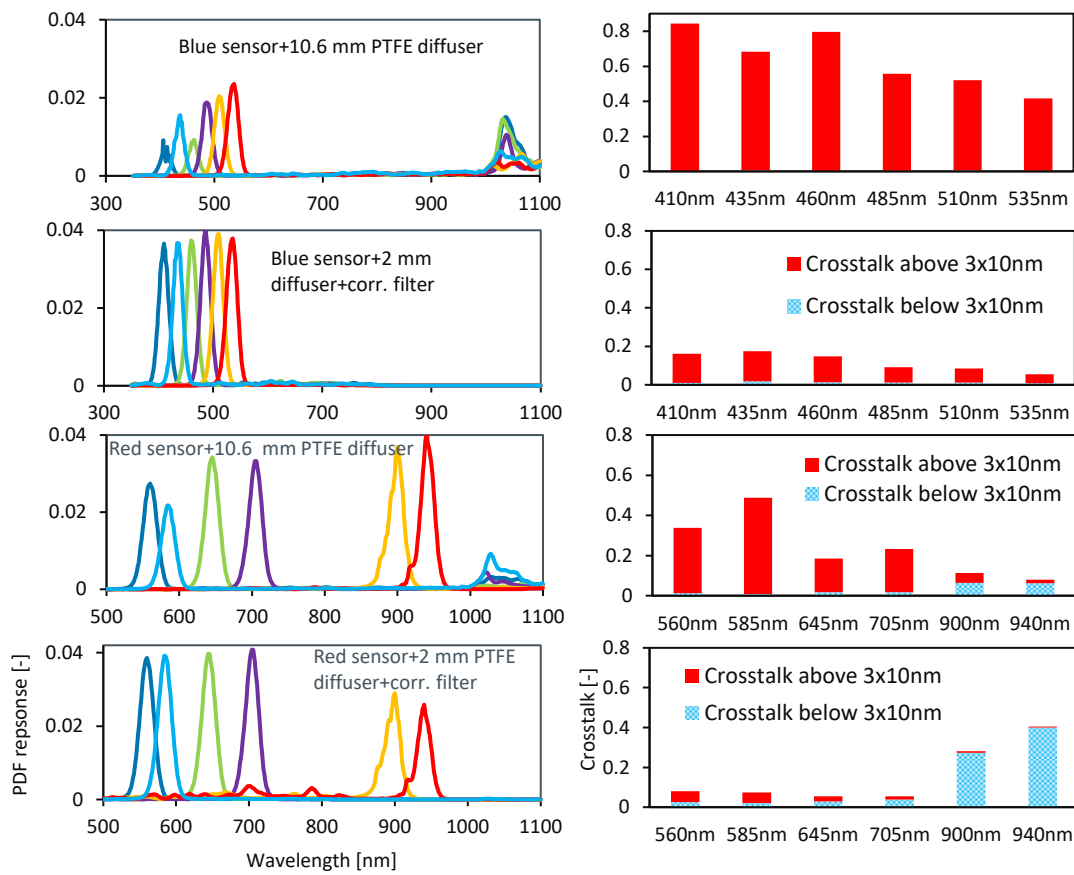
327 To remove infrared crosstalk, an optical short pass filter is required. However, a filter with a sharp cut-off
 328 at 1000 nm is, to our knowledge, not available or probably very expensive and sensitive to angle of
 329 incidence. Cost-effective short pass filters are made from heat-absorbing glass and have a dye added to
 330 the glass that absorbs infrared radiation. However, these heat-absorbing filters do not have a steep filter
 331 response and therefore ineffective to correct the red sensor without attenuating the 900 and 940 nm
 332 channels too much. The Schott heat-absorbing filters KG3 and KG1 appear to offer a good solution for
 333 the blue sensor (Fig. 7). The remaining crosstalk is mainly related to the slightly broader filter response.
 334 The first 4 channels of the red sensor (Fig. 6b) can also be improved. However, such a correction filter
 335 for the red sensor would increase crosstalk from shorter wavelengths for the 900 and 940 nm wavebands
 336 (see lower right panel in Figure 6b) and greatly reduce signal strength. For accurate PAR measurements,
 337 and when the 900 and 940 nm channel are not needed, it is recommended to use the weaker KG-1 filter
 338 for the red sensor.



339

340 Figure 7: Correction filters for the infrared crosstalk: Schott heat-absorbing filters (adapted from Schott
 341 AG manufacturer data).

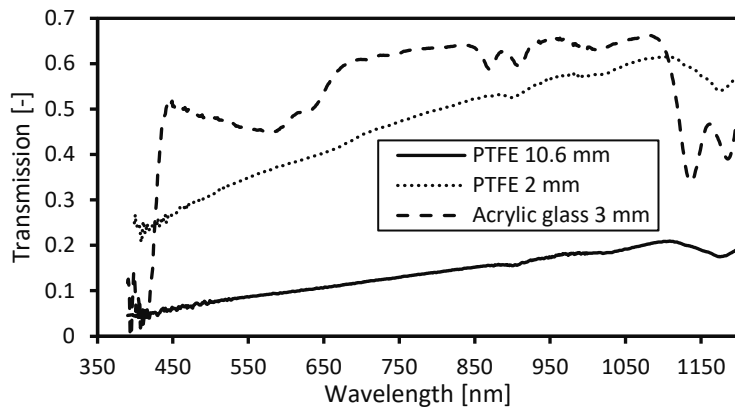
342



343

344 Figure 8: Spectral response and crosstalk (for a flat spectrum) of the blue and red sensor, without or
 345 with correction filter. First row: Blue sensor with 10.6 mm PTFE diffuser. Second row: Blue sensor with 2
 346 mm PTFE diffuser including a heat absorbing filter (Schott KG-3). Third row: Red sensor with 10.6 mm
 347 PTFE diffuser. Fourth row: Red sensor with 2 mm PTFE diffuser and heat absorbing filter (Schott KG-1),
 348 calculated from manufacturer data of sensor spectral response, transmission data of the Schott optical
 349 correction filter, and measured transmission of PTFE diffusers.

350 Because of the limited view angle of the spectroscopy sensors (40°), it is crucial to add a light diffuser.
 351 Two light diffusing materials were tested, PTFE and Opal cast acrylic sheet glass, and the transmission
 352 measurements are shown in Fig. 9 (measured with the ASD FieldSpec).

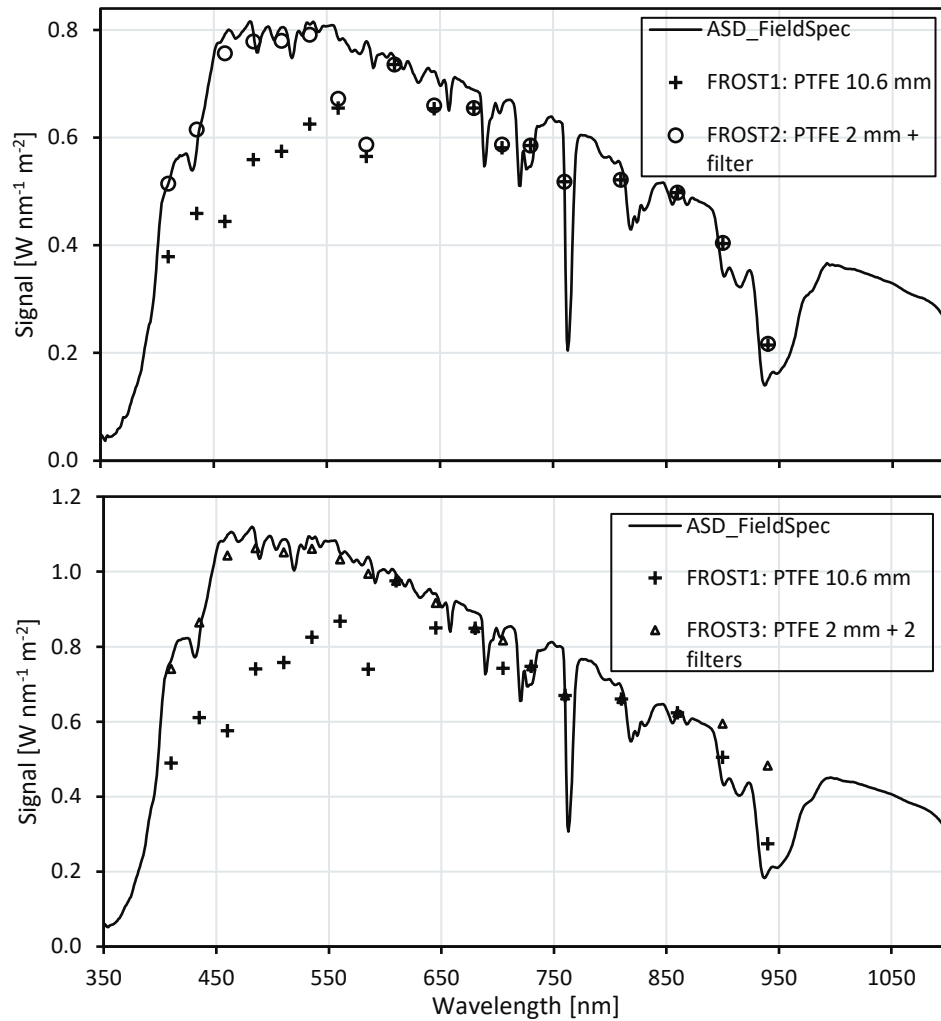


353

354 Figure 9: Transmission of PTFE diffusers and an Opal cast acrylic sheet glass diffuser measured with an
 355 ASD FieldSpec spectroradiometer.

356 The reduced transmittance of the PTFE diffusers in the shorter wavelengths enhances the near infrared
 357 crosstalk (see Fig. 6b top right panel and Fig. 8 top right panel). The combined effect of sensor and PTFE
 358 spectral response with or without correction filters is shown in Fig. 10. Three versions of the
 359 spectrophotometer were developed; one with a 10.6 mm PTFE diffuser to improve cosine response
 360 (FROST1), a second version with a 2 mm PTFE diffuser and a correction filter on the blue sensor
 361 (FROST2), and a third version with a 2 mm PTFE diffuser and correction filters on the blue and red
 362 sensor (FROST3). The spectral selective quality on real world measurements (Fig. 10) was calculated
 363 from the combined effect of the spectrophotometer filter characteristics (Fig. 6), diffuser (Fig. 9) and
 364 Schott correction filters (Fig. 7).

365



366

367 Figure 10: Outdoor measurements (ASD-FieldSpec) with calculated response of 3 FROST versions:
 368 FROST1 with a 10.6 mm diffuser, FROST2 with a 2 mm PTFE diffuser and a correction filter on the Blue
 369 sensor, and FROST3 with a 2 mm PTFE diffuser and a correction filter on the Blue and Red sensor,
 370 considering sensor spectral response and transmission of diffuser and correction filter, during clear sky
 371 conditions, Wageningen. Lower panel: 15 May 2022, 14:24 h UTC; upper panel: 11 March 2022, 13:35 h
 372 UTC.

373 Figure 10 shows that the first 6 channels, if uncorrected with a heat absorbing filter, underestimate the
 374 irradiance levels at the expected wavebands because these bands are very sensitive to the infrared
 375 region between 1000 and 1100 nm. At this infrared region, the solar radiation intensity is lower than
 376 what the blue sensor is supposed to see and thus leads to an underestimation of the Blue sensor for the
 377 visible channels. The heat-absorbing filters effectively remove this crosstalk. It also shows that the red
 378 sensor benefits from a heat absorbing filter for the wavebands 560 and 585 nm, but it greatly reduces
 379 the sensitivity of the 900 and 940 nm which makes the contribution of crosstalk from short wavebands
 380 too high (large positive deviation). Therefore the Red sensor should not be equipped with such a filter if
 381 the 900 and 940 nm wavebands are important, for example to estimate column atmospheric moisture
 382 (see Fig. 16).

383 The procedure to calibrate each waveband of FROST would require an accurate spectrophotometer and a
 384 clear day. First, each of the 18 PDF band responses of the sensor (with or without a correction filter!)
 385 and diffuser combination is multiplied with the known solar spectrum for a very clear day or measured
 386 with a calibrated spectrophotometer. This gives the nW m⁻² reference value that the FROST sensor
 387 should produce for each waveband. Subsequently the FROST raw 18 wavebands outputs are multiplied

388 by the AMS calibration factors (since we use the uncalibrated output for fast measurement) and divided
 389 by the reference values. The AMS spectroscopy sensor factory calibration values are written to the SD
 390 card at the very start of the measurements. The derivation of the calibration values for each FROST
 391 channel i in [Counts W⁻¹ m²] can be written as:

$$392 \quad Cal_{FROST,i} = \frac{Counts_i \cdot Cal_{manufacturer,i}}{\sum_{\lambda_1}^{\lambda_2} \left[\frac{R_{sensor_{i,\lambda}} \cdot T_{diffuser,\lambda} \cdot T_{filter,\lambda} \cdot Source_{\lambda}}{\sum_{\lambda_1}^{\lambda_2} R_{sensor_{i,\lambda}} \cdot T_{diffuser,\lambda} \cdot T_{filter,\lambda}} \right]} \quad (1)$$

393 where $Counts_i$ is the signal output of a Frost channel i , from 1 to 18, [-], $Cal_{manufacturer,i}$ is the
 394 manufacturer calibration factor [-] for channel i , $R_{sensor_{i,\lambda}}$ is the normalized peak spectral response of
 395 channel i [-] at wavelength λ [nm], $T_{diffuser,\lambda}$ is the spectral transmission of the diffuser [-] at wavelength
 396 λ [nm], $T_{filter,\lambda}$ is the transmission of the (optional) crosstalk correction filter [-] at wavelength λ [nm],
 397 $Source_{\lambda}$ [W m⁻²] is the output of the reference light source at wavelength λ [nm] (preferably the sun), λ_1
 398 and λ_2 are the lower and upper boundaries of the spectral sensitivity range (including crosstalk) of the
 399 FROST. Note that the denominator is the spectrally-weighted source-signal strength.

400

401 The sensor output sensitivity is then expressed as counts per (W m⁻²). The normalized sensor response is
 402 provided in Fig. 6 and 8 and in Table s1 in Supplementary Materials. An example of sensitivity values is
 403 presented in Table 2. These values were derived on 11 March 2022 13:35 UTC for the 10.6 mm diffuser
 404 version and the 2 mm diffuser + 1 filter version. The 2 mm diffuser with 2 correction filters was
 405 measured on 15 May 2022 (Fig. 10). Note that these values are only valid for an integration value of
 406 13.9 ms and a gain of 16. We do not recommend to use channels with Flag 2 or 3 if spectral accuracy is
 407 required.

408 Table 2: Sensitivity, or counts (C) per (W m⁻²) of FROST1, -2 and -3 with different configurations, offsets
 409 always zero. Every sensor uses a gain of 16 and an integration time of 13.9 ms. The flags denote quality
 410 of measurement (waveband accuracy). Flag 0: low crosstalk, Flag 1: crosstalk<20%, Flag 2:
 411 20%<crosstalk<35%, Flag 3: crosstalk>40%. The colors in the first column indicate each of the three
 412 sensors in a FROST. The final column shows the improvement factor on sensitivity when using a 3 mm
 413 white Acrylic glass diffuser instead of a 2 mm PTFE diffuser.

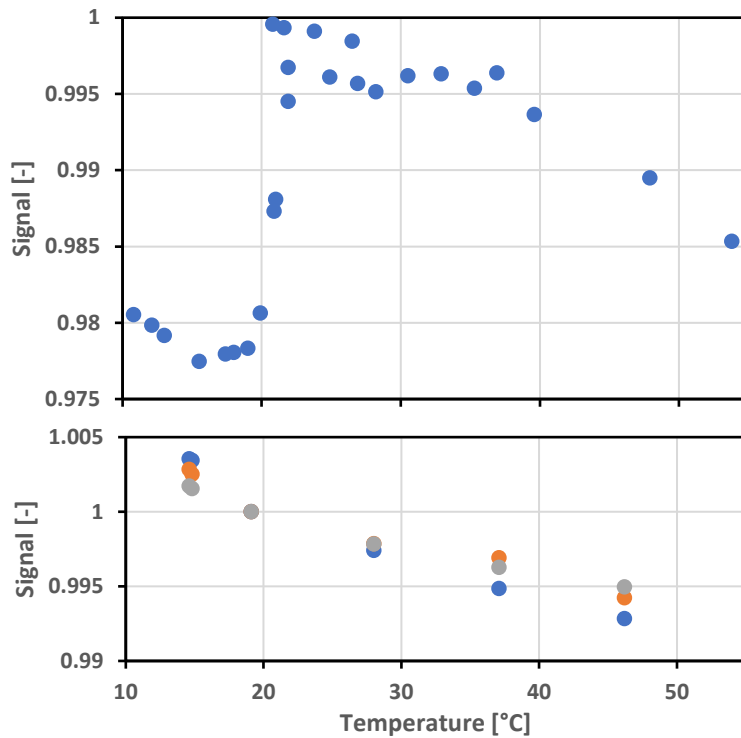
414

	FROST1		FROST2		FROST3		FROST_AG
Diffuser:	PTFE 10.6 mm		PTFE, 2 mm		PTFE, 2 mm		Acrylic glass, 3 mm
Filter:	no		on blue sensor		on blue and red sensor		Sensitivity increase
Waveband	Sensitivity		Sensitivity		Sensitivity		$\frac{T_{Acrylic\ glass_{3mm}}}{T_{PTFE_{2mm}}}$
	[nm]	[C W ⁻¹ m ²]	Flag	[C W ⁻¹ m ²]	Flag	[C W ⁻¹ m ²]	
610	116	0	474	0	494	0	1.61
680	132	0	503	0	436	0	1.49
730	156	0	549	0	554	0	1.39
760	156	0	413	0	387	0	1.36
810	188	0	673	0	651	0	1.31
860	194	0	760	0	649	0	1.25
560	51	2	253	2	186	0	1.70
585	70	2	333	2	195	0	1.65
645	55	1	256	1	168	0	1.56
705	70	1	295	1	117	0	1.43
900	90	0	348	0	19	3	1.12
940	107	0	395	0	25	3	1.20
410	94	3	153	0	157	0	1.55
435	100	3	200	0	206	0	2.38
460	144	3	211	0	218	0	2.08
485	96	3	209	0	217	0	1.94
510	94	3	213	0	221	0	1.85
535	84	3	204	0	213	0	1.76

415

416 **3.2 Temperature sensitivity and drift**

417 The diffuser and sensor were both tested for temperature effects. The measurements were corrected for
418 sensor temperature drift or drift in lamp output by measuring the lamp output with an extra sensor
419 outside the oven. The oven has an internal fan to assure a homogeneous temperature within the oven
420 chamber. The PTFE filter shows a significant jump in transmission around 21°C, then reaching a plateau
421 and slowly declining past 35°C (Fig. 12, upper panel). The temperature was slowly increased and
422 stabilized for 30 mins at each measurement point to minimize thermal delays in the PTFE material.



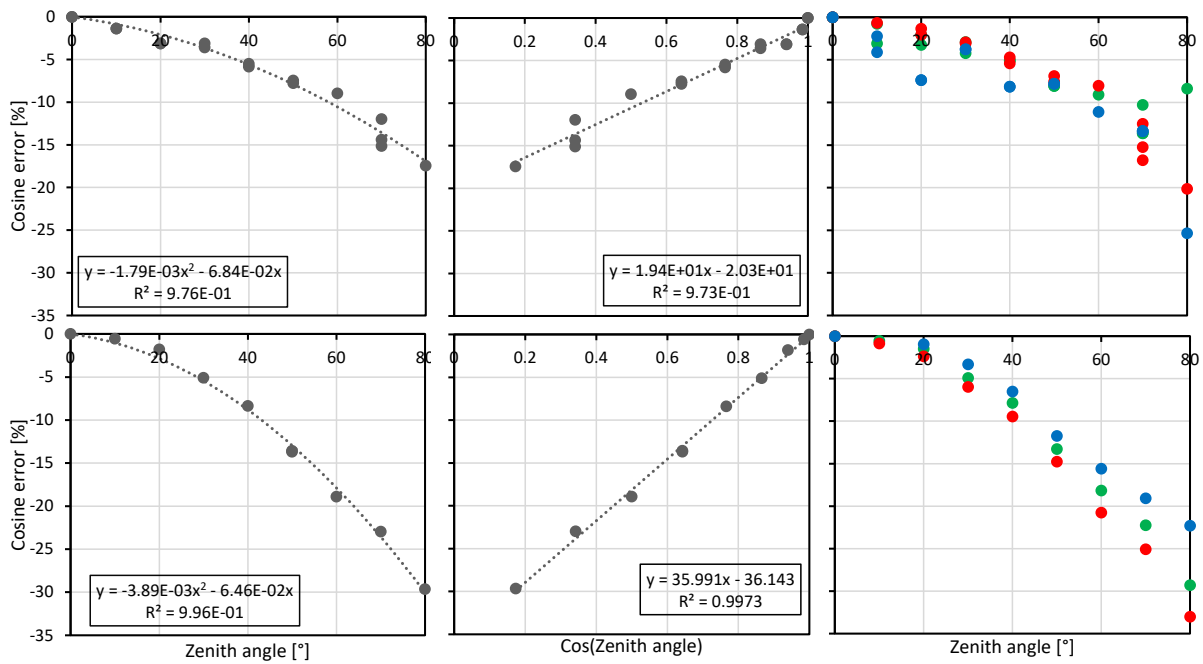
423

424 Figure 11: Temperature response; upper panel PTFE diffuser, lower panel 3 random light sensors (-250
425 ppm).

426 Three spectroscopy sensor chipsets (3x 18 waveband) were oven-tested for temperature sensitivity
427 between 16 to 46°C. Overall temperature sensitivity is -250 ppm K⁻¹ with a small variation among the
428 three sensors. Lower temperatures were not possible due to condensation issues when reaching the
429 dewpoint temperature of the laboratory (Fig. 11).

430 3.3 Cosine response and GHI

431 The cosine response measurements (outside, LED lamp) had a better performance for the 10 mm
432 diffuser but nevertheless had some inconsistencies among the three sensors. We tried to improve the
433 cosine response by leaving part of the sides uncovered but this caused a very high asymmetry among
434 the three sensors. The explanation is that the three sensors do not have the same viewing angle location
435 under the diffuser, thus some will see more from the side than the other sensors. The side sensitivity is
436 greatly reduced with a thinner filter but at the expense of a reduced cosine response (Fig. 12).



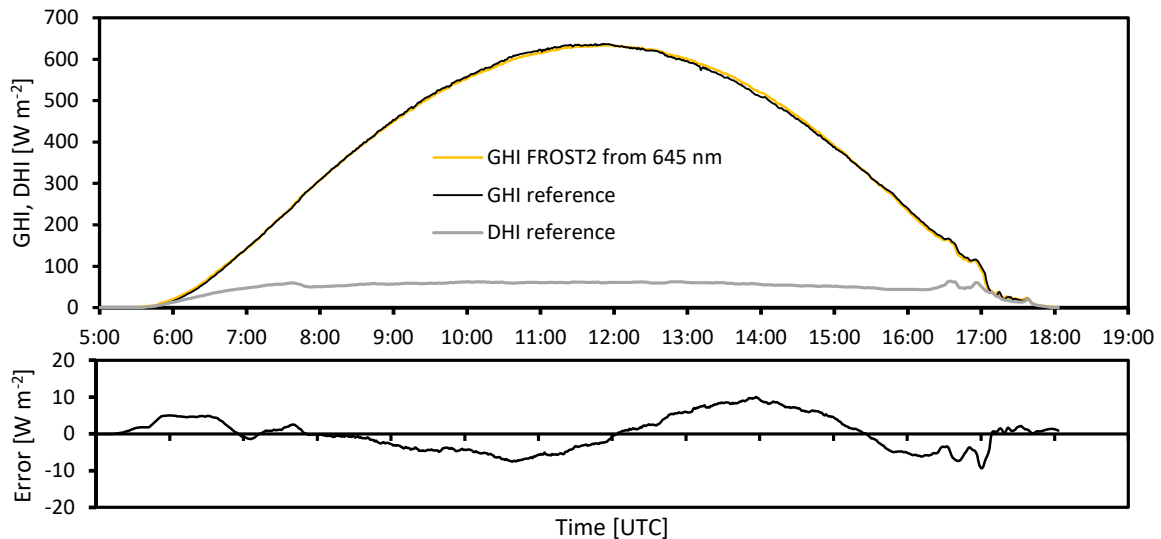
437

438 Figure 12: Upper graphs: 10.6 mm diffuser (black sides). Bottom graphs: 2 mm diffuser (sides painted
439 black). The right panels are color-coded for each sensor integrated circuit.

440 We found that most of the cosine response errors can be corrected afterwards and is demonstrated for
441 the 2 mm filter, which had the largest cosine response error but less transmission loss. The accurate
442 measurement of GHI can be achieved by first correcting for the zenith angle response (see Fig. 13,
443 middle lower panel) and subsequently applying a second order linear regression against a reference
444 pyranometer on one clear day (19 March 2021). Additionally, a correction for the limited spectral
445 response is needed. We tested this calibration method for the average signal of all 18 wavebands and on
446 single wavebands. The dataset contains clear sky days (Fig. 13), overcast days (Fig. 14) and rainy
447 weather (Fig. 15). The best overall results were achieved with either channel 645 or channel 705 nm,
448 with residual errors mainly below 10 W m^{-2} during contrasting weather conditions. Due to the spatial
449 separation of 156 m between our sensors and the reference solar radiation measurements and the
450 differences in response speed, we rejected the cloud passage time intervals. The 645 and 705 nm
451 wavebands seems to correct cloud effects on the GHI where irradiance is enhanced below 500 nm and
452 reduced due to water absorption bands at wavebands $>1 \mu\text{m}$.

453 The remaining uncertainty of the clear-day calibration (up to 10 W m^{-2} or 5%) is mainly related to small
454 levelling uncertainties or tolerances in input optics of both reference and our sensors. This is visible as a
455 shift from a negative to a positive bias around 12 UTC (Fig. 13).

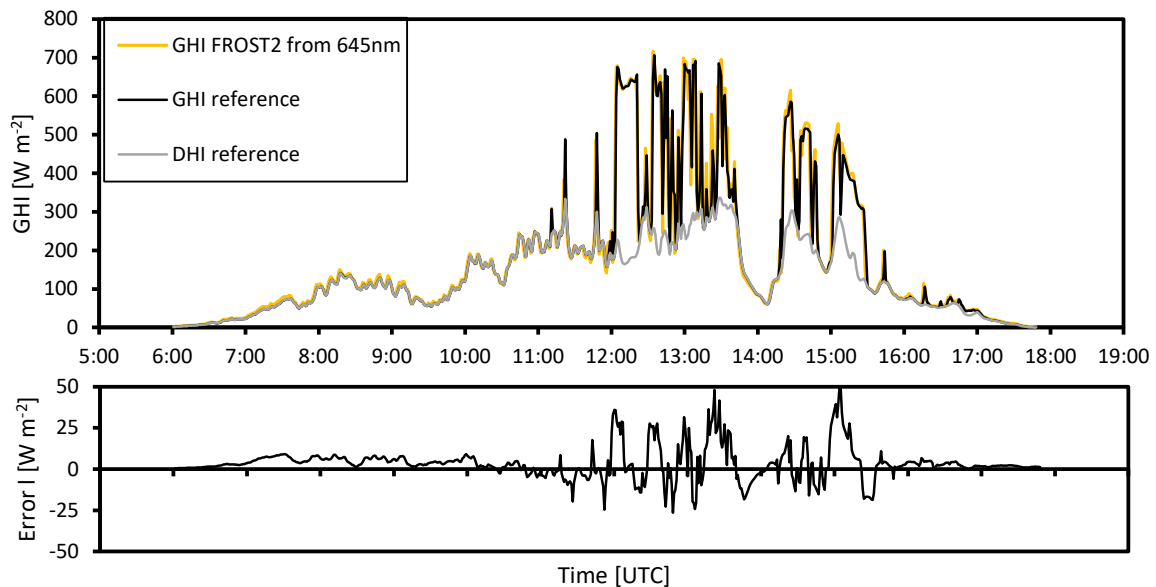
456



457

458 Figure 13: Comparison between GHI measured using a pyrheliometer and diffuse radiation sum (on a
 459 suntracker and correcting for zenith angle) and a calibrated FROST2 with 2 mm PTFE diffuser and 1
 460 correction filter, diffuse horizontal irradiance (DHI) measured with pyranometer mounted on a suntracker
 461 with shading ball, Veenkampen weather station, 19 March 2022. Relative errors at GHI >200 W m⁻² are
 462 <2% and mainly related to horizontal misalignment causing an asymmetric error before/after noon.

463

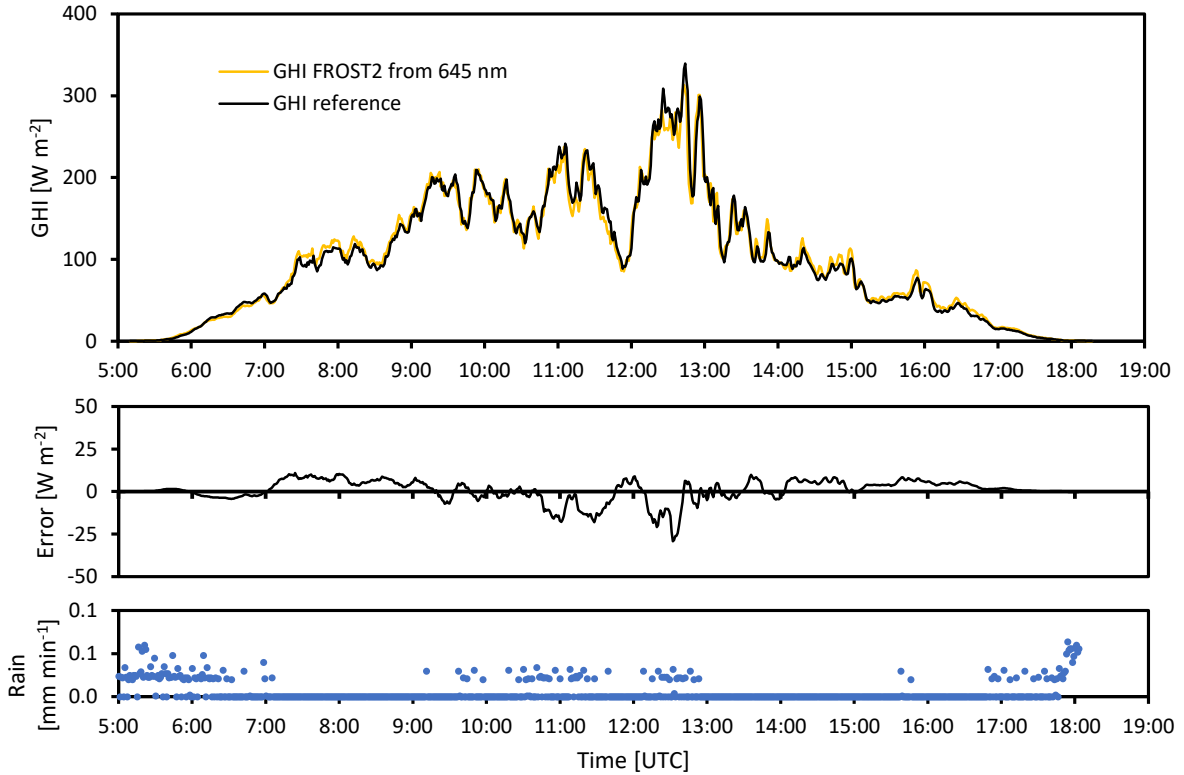


464

465 Figure 14: Calibrated FROST2 GHI from 645 nm (calibrated on a clear day, 19 March, see Fig. 13),
 466 calibration tested with cloudy weather conditions. Cloudy weather conditions in the morning, some
 467 clearing in the afternoon, 1 minute averaged data, error plot 10 min running mean to suppress
 468 differences due to spatial separation of FROST and reference (145 m apart), Veenkampen weather
 469 station, 14 March 2022. Relative errors at GHI >100 W m⁻² are <7% and mainly related to spatial
 470 separation between FROST and reference.

471

472



473

474 Figure 15: Calibrated FROST2 GHI from 645 nm (calibrated on a clear day, 19 March, see Fig. 13),
 475 calibration tested under rainy weather conditions, 1 minute averaged data, error plot 10 min running
 476 mean to suppress differences due to spatial separation of FROST and reference (145 m apart),
 477 Veenkampen weather station, 31 March 2022. Relative errors at GHI >100 W m⁻² are <7% and mainly
 478 related to spatial separation between FROST and reference.

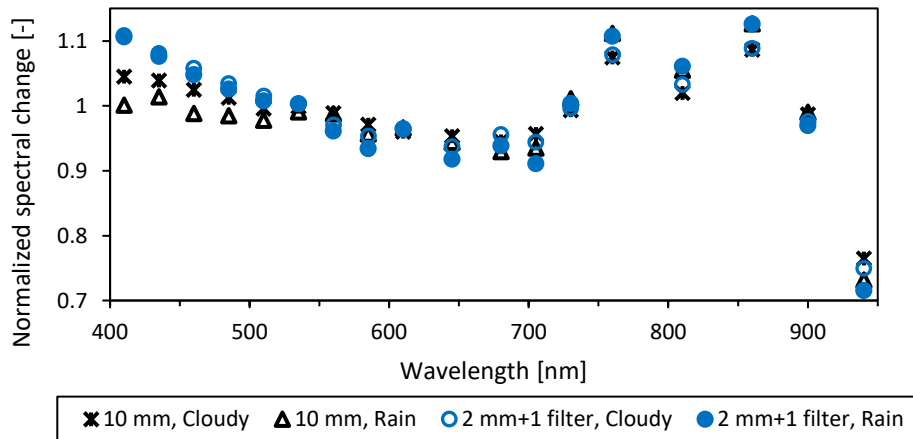
479 The instruments were not dried during the precipitation event (Fig. 15 and 16). Water droplets on the
 480 diffuser may affect light transmission and diffuser optical properties. Note that in Figs. 13-15, the
 481 nocturnal offsets are zero.

482 Next, we investigated how the light spectra is modified by clouds or rain. The two instruments, one with
 483 a 10 mm diffuser (FROST1) and the second version with a 2 mm diffuser and crosstalk correction filter
 484 on the blue sensor (FROST2), were used to calculate the spectral change due to cloudy or rainy weather
 485 conditions (Eq. 2).

486
$$\text{Spectral_change}_i = \frac{\frac{\text{Counts}_{i,\text{clouds_rain}}}{\frac{1}{18} \sum_{l=1}^{18} \text{Counts}_{l,\text{clouds_rain}}}}{\frac{\text{Counts}_{i,\text{clear}}}{\frac{1}{18} \sum_{l=1}^{18} \text{Counts}_{l,\text{clear}}}} \quad (2)$$

487 Data from the Figs. 13-15 experiments were used and, of the three contrasting days, the 11-12 UTC
 488 intervals were averaged and normalized for the average spectral signal of the 18 wavebands. Figure 16
 489 shows that the 940 nm waveband is very sensitive to moisture, with a reduction of more than 20% as
 490 compared to its nearest waveband. Accordingly, it can be used to derive information about atmospheric
 491 moisture such as column water vapor. Both cloudy and rainy conditions appear to modify the spectra in a
 492 similar way (Fig. 16). The low enhancement in the first four wavebands of the instrument with the 10
 493 mm diffuser version (FROST1) is related to the strong crosstalk in the near infrared. The corrected
 494 version with the 2 mm diffuser (FROST2), which contains the crosstalk correction filter, shows an
 495 enhancement due to clouds and in line with the findings by Durand et al., 2021, who had an
 496 enhancement below 465 nm. The 645 or 705 nm as shown in Figs. 13-15 appear to have the right
 497 amount of sensitivity reduction due to clouds and rain (slightly stronger) to be used for GHI
 498 measurements. It is, however, recommended to use all 18 bands and use a proper weighting function

499 that reduces sensitivity in the visible region. We currently have no explanation for the enhancements
500 between 750 and 860 nm.

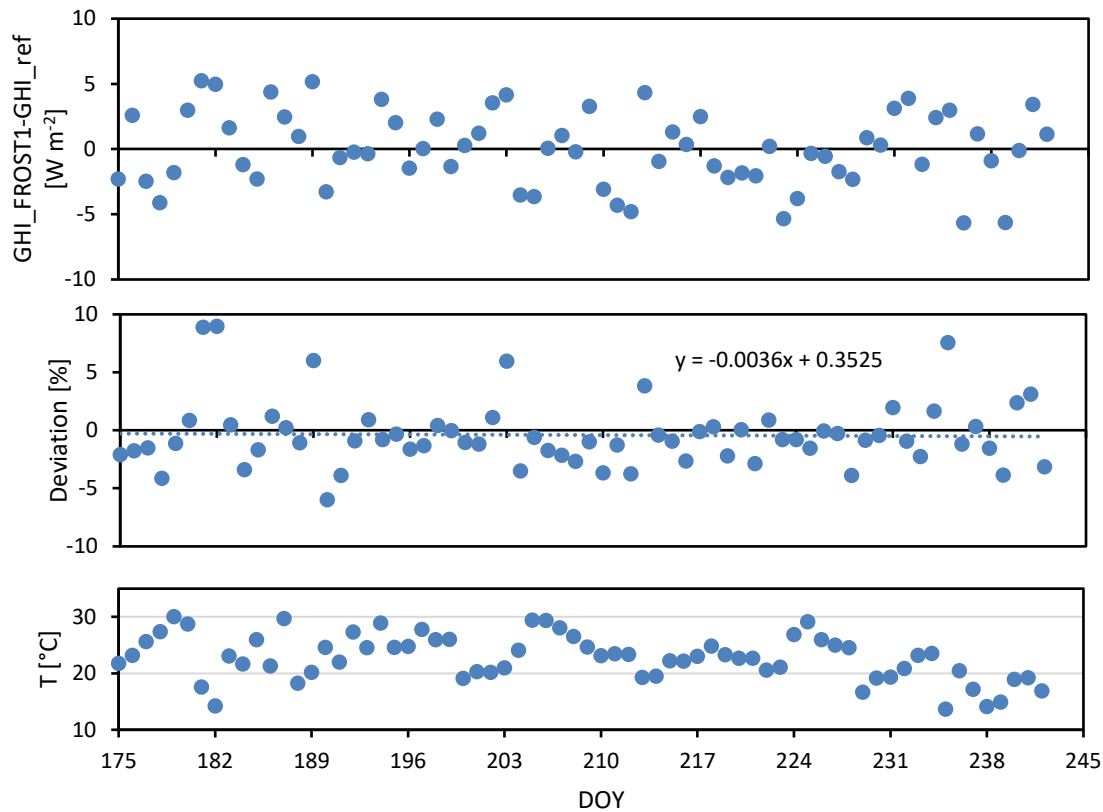


501

502 Figure 16: Two FROST instruments, one with a 10 mm diffuser (FROST1) and one with a 2 mm diffuser
503 and correction filter (FROST2). The normalized spectral cloud modification factor, is the spectral change
504 of cloudy (14 March, 2022) and rainy weather (31 March, 2022) compared to a cloud-free day (19 March
505 2022), Veenkampen weather station, data averaged between 11 and 12 UTC for each day.

506 The long-term drift was tested at the Lindenberg rooftop observatory. One instrument was measuring
507 from 22 June to 31 August 2021 (without any missing 0.1 s measurements). These 2.5 months of data
508 were converted to GHI values by using only one relatively clear day (13th August) and compared with
509 their reference pyranometer. The GHI standard error was 2.5 W m^{-2} for daily averages with a diffuser
510 temperature correction obtained by increasing sensor values by 2% at temperatures below 21°C
511 according to Fig. 11 and cosine response correction according to Fig. 12 upper panel (for daily errors see
512 Fig. 17 upper panel). Additionally, the GHI deviations in percentage between 12 and 13 h UTC were
513 averaged to reveal possible sensor drift in time. The diffuser correction practically removed all long-term
514 drift (Fig. 17, middle panel).

515



516

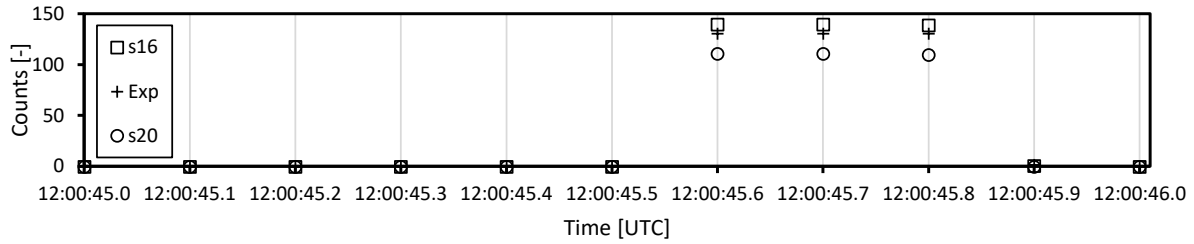
517 Figure 17: Long-term stability of FROST1 GHI measurements (using the 645 nm channel and calibrated
 518 with DOY 226, 14 August data). Upper panel: daily average FROST GHI deviation from reference GHI.
 519 Middle panel: FROST1 GHI deviation from averaged data between 12 and 13 h UTC. Lower panel:
 520 average air temperature between 12 and 13 h UTC, during a 2.5 month comparison experiment at
 521 Lindenberg. Measurements corrected for PTFE diffuser transmission change at 21°C.

522

523 **3.4 Spatial measurements and synchronization**

524 For spatial measurements, exact synchronization is essential. Our GNSS solution uses the hardware
 525 timing pulse of the GNSS to trigger a measurement. To illustrate the synchronization performance we
 526 set-up three stand-alone FROST sensors and let them run for 1 h outdoors. We then placed them in a
 527 dark room and at 12:00:45.6 UTC a LED light source was switched on for 0.3 s. Figure 18 shows 1.1 s of
 528 collected 10 Hz data of the 610 nm waveband. The response appears instantaneous and perfectly
 529 synchronized. There is still an integration time for each measurement and this was set at 13.9 ms for
 530 FROST s16 and s20 and, for testing purposes, twice as long for the experimental version with a less
 531 transparent diffuser to get more signal. This instrument is denoted with "Exp" in Fig. 18. Therefore, the
 532 "Exp" FROST occasionally showed a small delay and illustrates the importance of configuring all sensors
 533 with the same integration time. Figure 18 also shows that the instruments have no zero offset (no dark
 534 current) errors.

535



536

537 Figure 18: Example of synchronization, response speed and zero offsets of three standalone instruments
 538 (uncalibrated). All three use their own GNSS for synchronization. Light pulse of 0.3 s generated by a LED
 539 lamp.

540 The full sensor readout requires two integration cycles with each cycle measuring 12 channels (see Table
 541 3). As a result, there is a maximum of one integration cycle delay between certain channels (with our
 542 default settings: maximum 28 ms). Six channels are measured twice within one default measurement
 543 cycle (Table 3). For critical synchronization applications, it is possible to measure only 12 of the 18
 544 channels during each measurement cycle.

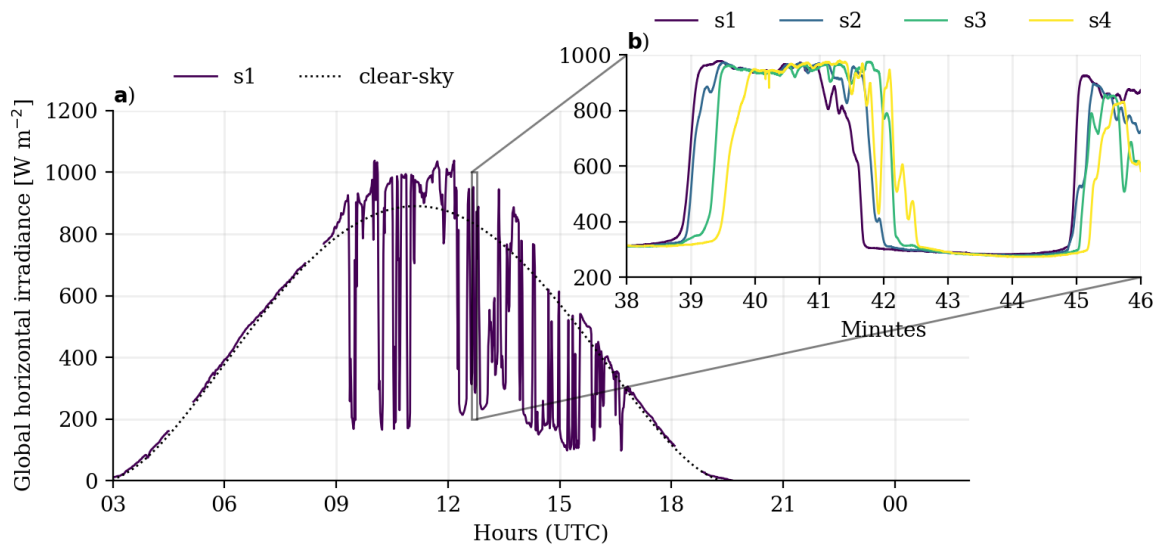
545 Table 3: Readout order during one full measurement cycle.

R	S	T	U	V	W	G	H	I	J	K	L	A	B	C	D	E	F
610nm	680nm	730nm	760nm	810nm	860nm	560nm	585nm	645nm	705nm	900nm	940nm	410nm	435nm	460nm	485nm	510nm	535nm
		1	1	1	1		1	1	1		1		1	1	1		1
	2		2	2		2	2	2		2		2	2	2		2	2

546

547 The downside of a fast integration cycle is a smaller output signal. The 10.6 mm diffuser reduces the
 548 light onto the detector significantly, approximately 120 to 30 counts per channel at 650 W m^{-2} . The 2
 549 mm diffuser increases the signal by a factor of four. Longer integration times are considered but should
 550 be less than 50 ms to assure a sustained 10 Hz output (two integration cycles < 100 ms). Additional time
 551 is needed for data communication. The AMS spectroscopy sensor output is in ASCII format and therefore
 552 more digits require more time to transmit.

553 For the measurement campaign in Falkenberg, a large 2D sensor grid was deployed with a 50 m grid
 554 spacing. It is a good illustration of the spatial dynamics of GHI during partly-cloudy conditions. The 1 min
 555 averaged data at one point shows the cloud enhancements and the 10 Hz measurements show the high
 556 dynamics and spatial variation along a 150 m transect (Fig. 19).



557

558 Figure 19: 10 Hz measurements of spatial variation of GHI at four locations along a 150 m west-east
 559 transect (b) compared to one location (a) at 1 minute averages. The dashed line shows the CAMS
 560 McClear clear-sky product. Falkenberg, 27 June, 2021.

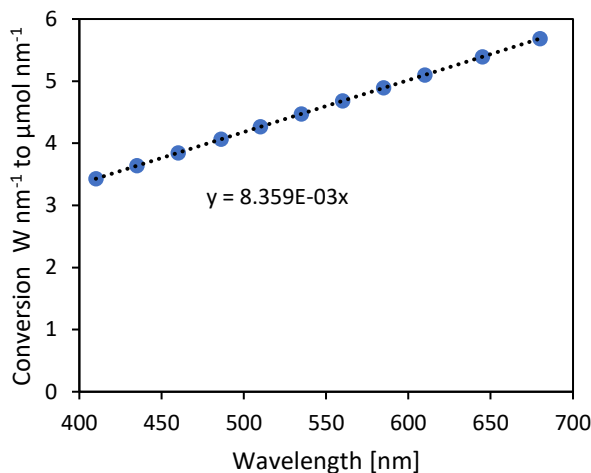
561 **3.5 Photosynthetic Active Radiation**

562 Sensors for measuring Photosynthetic Active Radiation (PAR) are usually constructed using a silicon
 563 photo diode and a light bandpass filter from 400 to 700 nm. Photosynthesis is a quantum process and
 564 therefore measurement are usually expressed as a Photosynthetic Photon Flux Density (PPFD, μmol
 565 $\text{photons m}^{-2} \text{s}^{-1}$). The sensor therefore must account for the larger number of photons at larger
 566 wavelengths. The wavelength sensitivity (per $\text{W m}^{-2} \text{nm}^{-1}$) is such that the sensitivity at 700 nm
 567 wavelength is 1.75 times larger than at 400 nm. In our case, we have 11 well-defined wavebands within
 568 the PAR region. Therefore, a digital filter can be used to calculate PPFD. Since the sensor outputs in W m^{-2}
 569 nm^{-1} , it must be converted to PPFD by calculating the number of moles per joule per waveband.

570 The photon energy (E_n) at each waveband (n) is related to wavelength (λ) by the speed of light (c) and
 571 the Planck constant (h): $E_n = \frac{hc}{\lambda_n}$. The photons (P) per m^2 are: $P_n = \frac{R_n}{E_n}$, where R_n is the irradiance measured
 572 at each waveband. The number of moles is linked to the number of photons through Avogadro's number
 573 (A) and integration over all FROST3 11 wavebands yields the total PPFD:

574
$$PPFD = (700 - 400) \int_{n=1}^{11} P_n / A n_{max} \tag{2}$$

575



576

577 Figure 20: Conversion factor for each FROST3 waveband to calculate PPFD [$\mu\text{mol m}^{-2} \text{s}^{-1}$].

578 The translation factor from $\text{W m}^{-2} \text{nm}^{-1}$ to $\mu\text{mol m}^{-2} \text{s}^{-1} \text{nm}^{-1}$ for the 11 wavebands is depicted in Fig. 20.
 579 The PPFD in Figure 10, lower panel, according to Eq. 2 is for example $1293 \mu\text{mol m}^{-2} \text{s}^{-1}$.

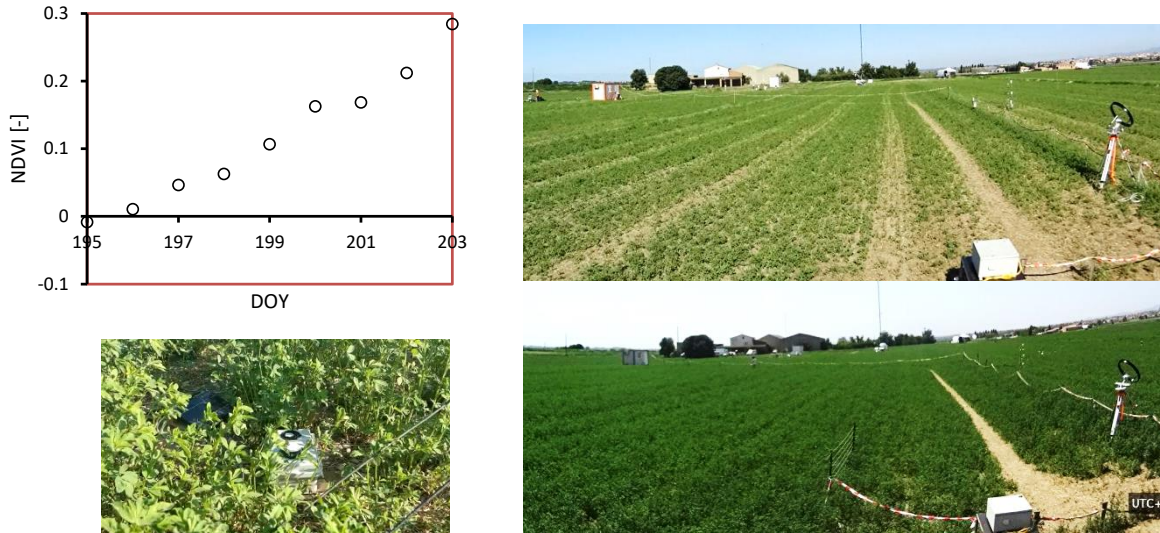
580 Note that the 11 channels within the PPFD range of FROST3 can be used to study vegetation specific
 581 photosynthesis spectral response.

582 **3.6 Vegetation development**

583 The FROST was tested during a field experiment in La Cendroza, Spain (Lat: 41.692537, Long:
 584 0.931540) (Liaise Campaign, Boone et al., 2021) from 14-22 July 2021. The instrument was placed on
 585 the bare soil surface at the moment the Alfalfa vegetation started to develop. The Normalized Difference
 586 Vegetation Index (NDVI) index $(\text{NIR}-\text{VIS})/(\text{NIR}+\text{VIS})$ is used in remote sensing to quantify crop growth;
 587 a low value is bare soil and a value of 1 represents a full-grown crop. It can be computed from at least

588 two wave bands, one in the near infrared (>700 nm) and a second waveband in the visible range. The
 589 two wave bands 680 and 730 nm in version 1 are not affected by infrared crosstalk and both measure at
 590 the same sensor chip to assure that both channels have the same viewing angle. Figure 21 shows daily
 591 values of NDVI.

592



593

594

595

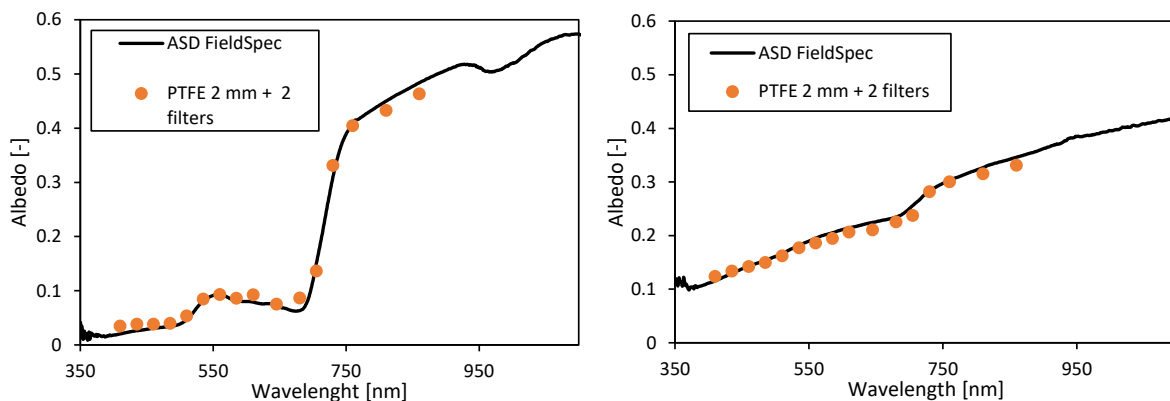
596

597 Figure 21: NDVI measurements calculated from FROST1 (with 10 mm diffuser) 680 and 730 nm
 598 wavebands located inside an alfalfa canopy. Bottom left: FROST (top at about 8 cm height) placed on the
 599 surface in between alfalfa, crop height 30 cm, (18 July). Top right: alfalfa crop on 14 July (crop height 23
 600 cm). Bottom right: alfalfa crop (height 48 cm) on 22 July; Spain from 14-22 July 2022.

601 **3.7 Surface albedo**

602 A good test for the quality of the spectral measurements without having to deal with absolute calibration
 603 uncertainties are surface reflectance measurements. The typical spectral reflectance signature of a
 604 healthy vegetation has two minima in the visible range at 500 and 675 nm and a small peak at 550 nm.
 605 Beyond 750 nm it is strongly reflective (about 50%). A bare soil surface, in this case a sandy soil patch
 606 from a very deep soil layer that surfaced during the recent drilling of a well at the weather station,
 607 served as a bare soil plot and had a negligible organic soil fraction. The ASD FieldSpec was equipped with
 608 a cosine collector and operated in irradiance mode. Weather conditions were sunny with low soil moisture
 609 content of the bare soil. The comparison is good considering the difficulty of sampling the same spot for
 610 both instruments due to differences in cosine response, size of sensor head and levelling (Fig. 14).

611



612 Figure 22: Spectral reflectance as measured by the FROST3 and the ASD FieldSpec with cosine collector.
613 Left panel: spectral reflectance of grassland, Veenkampen weather station, 14:12 UCT 15 May 2022,
614 Right panel: sandy soil (dry, no organic fraction), 14:06 UTC 15 May 2022.

615 The small underestimation of the 810 and 860 nm channels is related to the small cross correlation with
616 smaller wavelengths (Fig. 22).

617 **4. Concluding remarks**

618 The FROST instrument will enable new research opportunities. It is much faster than traditional
619 thermopile pyranometers and the low cost enables the deployment of large sensor grids. It can be
620 deployed very quickly because it is a fully stand-alone, “plug and play” solution and measurements are
621 always fully synchronized to UTC within at least a μs . The instrument has superior linearity ($<0.2\%$), the
622 temperature coefficient is very low (-250 ppm K^{-1}), and was consistent among the three tested
623 instruments. In contrast to thermopile sensors, the FROST has no zero-offset errors. The drift with time
624 appeared insignificant during a 2.5 month field test. Compared to PAR sensors, FROST can resolve the
625 PAR spectra in 11 narrow wavebands (FWHM: 20 nm). This makes it possible to study wavelength
626 dependent photosynthesis responses of, for example, chlorophyll A and B. This is also relevant in canopy
627 profile studies where solar irradiance extinction through a canopy modifies its light spectra. The fast
628 response makes it possible to investigate the impact of the growth and wind induced movements of
629 vegetation on radiation fluctuations.

630 FROST measures GHI in 18 wavebands and includes a water absorption band, which makes it possible to
631 derive information about atmospheric moisture such as column water vapor. Additionally, by using
632 proper infrared crosstalk correction filters, it can monitor the spectral reflection properties of a surface
633 with its first 16 wavebands from 410 to 860 nm. FROST can also be used to monitor vegetation growth
634 by measuring NDVI.

635 We hope that other researchers will benefit from our crosstalk problem solution. Tran and Fukazawa
636 (2020), used the same AMS spectroscopy sensor to determine optical properties of fruit, but they did not
637 use LED light sources as recommended by the manufacturer. Their halogen light source emits much
638 infrared light $>1000 \text{ nm}$ and therefore the 6 channels of their blue sensor and 2 of their 6 red sensor
639 channels were greatly affected by infrared crosstalk. This is something they may not have been aware of
640 because the AMS spectroscopy sensor datasheet does not show the filter response above 1000 nm. We
641 believe their instrument performance would improve using our proposed correction filters.

642 Although the proposed cosine correction appears to give good results (2.5 W m^{-2} standard error for daily
643 averaged GHI), we will continue to improve the cosine collector for large zenith angles. PTFE as a diffuser
644 material has better transmission properties below 400 nm than opal cast Acrylic sheet glass, but it
645 exhibits a 2% step wise increase in transmission beyond 21°C . Since the shortest waveband sensitivity
646 of the FROST sensor is limited to 400 nm (considering FWHM), we recommend using opal cast Acrylic
647 glass diffusers for future versions. This would also remove UV radiation exposure and reduce sensor
648 aging.

649

650 **Author contributions**

651 B.H. wrote the manuscript draft, methodology of synchronization, fast spatial spectral irradiance
652 measurements, instrument software, electronics and mechanical design, investigation and visualization
653 of spectral response, thermal sensitivity; W.M. organized the Germany and Spain field campaigns
654 including data organization and visualization of 2D performance in Fig. 19; W.M. and B.H. did the cosine
655 collector and long-term stability experiments and analysis; C.v.H. is the PI of the Shedding Light On
656 Cloud Shadows (SLOCS) project to which this research belongs and designed the research programme
657 that depends on this instrument; W.M. and C.v.H. reviewed and edited the manuscript.

658 **Acknowledgements**

659 We are grateful for the support and use of the optical calibration facility of DWD Lindenberg and many
660 thanks go to Stefan Wacker and Steffen Gross. We also thank Harm Bartholomeus (Wageningen
661 University, Remote sensing group) for providing the ASD FieldSpec and Emilie Wientjes (Wageningen
662 University) for assistance with their Cary 4000 UV-Vis spectrophotometer. Simon Berkowicz is thanked
663 for his valuable input and proofreading.

664 C.v.H., W.M., and B.H. acknowledge funding from the Dutch Research Council (NWO) (grant:
665 VI.Vidi.192.068).

666

667 **References**

668 Alados-Arboleda, L., Batles, F.J., Olmo, F.J.: Solar radiation resource assessment by means of silicon
669 cells, *Solar Energy*, 54-3, 183-191, [https://doi.org/10.1016/0038-092X\(94\)00116-U](https://doi.org/10.1016/0038-092X(94)00116-U), 1995.

670 Boone, A., Bellvert, J., Best, M., Brooke, J., Canut-Rocafort, G., Cuxart, J., Hartogensis, O., e Moigne, P.,
671 Miró, J. R., Polcher, J., Price, J., Quintana Seguí, P., & Wooster, M.: Updates on the International Land
672 Surface Interactions with the Atmosphere over the Iberian Semi-Arid Environment (LIAISE) Field
673 Campaign. *GEWEX News*, 31(4), 17–21, 2021.

674 Cahalan, R.F., Oreopoulos, L., Marshak, A., Evans, K.F., Davis, A.B., Pincus, R., Yetzer, K.H., Mayer, B.,
675 Davies, R., Ackerman, T.P., Barker, H.W., Clothiaux, E.E., Ellingson, R.G., Garay, M.J., Kassianov, E.,
676 Kinne, S., Macke, A., O'hirok, W., Partain, P.T., Prigarin, S.M., Rublev, A.N., Stephens, G.L., Szczap, F.,
677 Takara, E.E., Wen, T.V.G., Zhuravleva, T.B.: THE I3RC: Bringing Together the Most Advanced Radiative
678 Transfer Tools for Cloudy Atmospheres. *Bull. Am. Meteorol. Soc.*, 86-9, 1275-1293,
679 <https://doi.org/10.1175/BAMS-86-9-1275>, 2005.

680

681 Driemel, A., Augstine, J., Behrens, K., Colle, S., Cox, C., Cuevas-Agulló, E., Denn, F.M., Duprat, T.,
682 Fukuda, M., Grobe, H., Kustov, V., Long, C.N., Longenecker, D., Lupi, A., Maturilli, M., Mimouni, M.,
683 Ntsangwane, L., Ogihara, H., Olano, X., Olefs, M., Omori, M., Passamani, L., Pereira, E.B., Schmithüsen,
684 H., Schumacher, S., Sieger, R., Tamlyn, J., Vogt, R., Vuilleumier, L., Xia, X., Ohmura, A., König-Langlo,
685 G.: Baseline Surface Radiation Network (BSRN): structure and data description (1992-2017). *Earth Syst.*
686 *Sci. Data*, 10, 1491-1501, <https://doi.org/10.5194/essd-10-1491-2018>, 2018.

687

688 Durand, M., Murchie, E.H., Lindfors, A.V., Urban, O., Aphalo, P.J., Robson, M.: Diffuse solar radiation and
689 canopy photosynthesis in a changing environment. *Agricultural and Forest Met.*, 311, Article 108684,
690 <https://doi.org/10.1016/j.agrformet.2021.108684>, 2021.

691 Guichard, F. and Couvreur, F.: A short review of numerical cloud-resolving models. *Tellus A: Dynamic*
692 *Meteorology and Oceanography*, 69:1, 1373578, <https://doi.org/10.1080/16000870.2017.1373578>,
693 2017.

694 Kreuwel, F. P. M., Knap, W. H., Visser, L. R., Sark, W. G. J. H. M. van, Vilà-Guerau de Arellano, J.,
695 Heerwaarden, C. C. van: Analysis of high frequency photovoltaic solar energy fluctuations. *Solar Energy*
696 206: 381-389, <https://doi.org/10.1016/j.solener.2020.05.093>, 2020.

697 Lohmann, G. M.: Irradiance variability quantification and small-scale averaging in space and time: a
698 short review. *Atmosphere* 9 (7): 264. <https://doi.org/10.3390/atmos9070264>, 2018.

699 Lopes Pereira, R., Trindade, J., Gonçalves, F., Suresh, L., Barbosa, D., Vazão, T.: A wireless sensor
700 network for monitoring volcano-seismic signals. *Nat. Hazards Earth Syst. Sci.*, 14: 3123-3142,
701 <https://doi.org/10.5194/nhess-14-3123-2014>, 2014.

702 Michalsky, J.J., Perez, R., Harrison, L., LeBaron, B.A.: Spectral and temperature correction of silicon
703 photovoltaic solar radiation detectors. *Solar Energy*, 47, No. 4: 299-305, [https://doi.org/10.1016/0038-](https://doi.org/10.1016/0038-092X(91)90121-C)
704 [092X\(91\)90121-C](https://doi.org/10.1016/0038-092X(91)90121-C), 1991.

705 Nann, S. and Riordan C.: Solar spectral irradiance under clear and cloudy skies: measurements and a
706 semiempirical model, *J. Appl. Meteor.*, 21:447-462, [https://doi.org/10.1175/1520-](https://doi.org/10.1175/1520-0450(1991)030<0447:SSIUCA>2.0.CO;2)
707 [0450\(1991\)030<0447:SSIUCA>2.0.CO;2](https://doi.org/10.1175/1520-0450(1991)030<0447:SSIUCA>2.0.CO;2), 1991.

708 Tran, N.T., and Fukuzawa, M.: A portable spectrometric system for quantitative prediction of the soluble
709 solids content of apples with a pre-calibrated multispectral sensor chipset. *Sensors*, 20: 5883,
710 <https://doi.org/10.3390/s20205883>, 2020.

711 Veerman, M.A., Pedruzo-Bagazgoitia, X., Jakub, F., Vilà-Guerau de Arellano, J., Heerwaarden, C.C. van,
712 2020: Three-dimensional radiative effects by shallow cumulus clouds on dynamic heterogeneities over a
713 vegetated surface. *Journal of Advances in Modeling Earth Systems*, 12,
714 <https://doi.org/10.1029/2019MS001990>, 2020.

715 Yliantilla, L. and Schreder, S., 2005: Temperature effects of PTFE diffusers. *Optical Materials*, 27, 1811-
716 1814, <https://doi.org/10.1016/j.optmat.2004.11.008>, 2004.

717 Yordanov, G.H., Saetre, O., Midtgard, O.: 100-millisecond resolution for accurate overirradiance
718 measurements. *IEEE Journal of Photovoltaics*, 3, 1354-1360,
719 <https://doi.org/10.1109/JPHOTOV.2013.2264621>, 2013.

720 Yordanov, G.H., A study of extreme overirradiance events for solar energy applications using NASA's
721 13RC Monte Carlo radiative transfer model. *Solar Energy*, 122, 954-965,
722 <https://doi.org/10.1016/j.solener.2015.10.014>, 2015.

723

724